7 Orbital Mechanics of Propellantless Propulsion Systems

COLIN R. MCINNES[1] AND MATTHEW P. CARTMELL[2]

[1]*Department of Mechanical Engineering, University of Strathclyde*
[2]*Department of Mechanical Engineering, University of Glasgow*

Contents

7.1 Introduction

Conventional spacecraft are limited in their ability to deliver high-energy missions by a fundamental reliance on reaction mass. However, this constraint can in principle be overcome by a class of propellantless propulsion systems which either extract momentum from the environment (solar sails) or balance momentum through payload exchanges (tethers). This chapter provides a brief introduction to the physics of solar sail and tether propulsion systems, an analysis of some novel aspects of their orbital mechanics and a review of potential applications.

The classical rocket equation starkly illustrates the limitations of reaction propulsion, through an exponential scaling of initial mass m_1 with mission ΔV for some delivered mass m_2, such that $m_1 = m_2 \exp(\Delta V / g_o I_{sp})$, where I_{sp} is the specific impulse of the propulsion system ($g_o = 9.81 \, \mathrm{ms}^{-2}$). Attempts to overcome this scaling law rely on improved propulsion technologies (higher specific impulse) or reducing payload mass through miniaturisation. While such approaches have been successful, as evidenced by recent flight tests of solar electric propulsion, the envelope of possible missions is still constrained by the reliance on a finite mass of propellant.

Solar sailing could overcome the limitations of the rocket equation by extracting momentum from the flux of photons which is continually emitted by the Sun. A large articulated reflector is used to reflect photons, changing their momentum, and so exerting a reaction force on the sail. For an ideal solar sail, the net force exerted by incident

and reflected photons is normal to the sail surface. Therefore, by rotating the sail, the thrust vector can be directed in a hemisphere about the Sun-sail line. However, due to the reduction in projected sail area and the reduction in the component of photon momentum transferred normal to the sail, the magnitude of the thrust decreases rapidly as the sail normal is pitched away from the Sun-sail line. It can be shown that the thrust magnitude scales as $(\hat{\mathbf{r}}.\mathbf{n})^2$, where $\hat{\mathbf{r}}$ is the unit vector directed along the Sun-sail line and $\mathbf{n}$ is the unit vector normal to the sail surface. By rotating the sail, the solar sail can either gain or lose orbital angular momentum and so can spiral inwards towards the Sun or outwards away from the Sun. In addition, by pitching the sail such that a component of the thrust is directed out of the orbit plane, the solar sail orbit inclination can be 'cranked' up or down, allowing a rendezvous with any target body in the solar system. While solar sailing appears to enable new high-energy missions and exotic highly non-Keplerian orbits, challenges are posed to engineer a sail assembly with a low areal density which can be reliably deployed in-orbit.

Tethers also attempt to overcome the limitations of the rocket equation, by balancing the flow of momentum through the tether system. While future concepts for orbital towers offer the possibility of truly low cost access to space, nearer term concepts for momentum exchange tethers can enable the transfer of large payloads to and from low Earth orbit, without the use of propellant. In particular, staged tethers can allow the transfer of mass from low Earth orbit to a rotating tether orbiting the moon, which delivers the payload to the lunar surface. If mass is also transferred from the lunar surface back to low Earth orbit, then in principle the flow of momentum is balanced, allowing the tether transportation system to operate without the use of reaction mass.

In summary, both solar sails and momentum exhange tethers can, in principle, overcome the fundamental limitations imposed by reaction propulsion. For solar sails, new high-energy mission concepts are enabled, along with families of exotic highly non-Keplerian orbits described in this chapter. For momentum exchange tethers, large payloads can be transported at low cost by balancing the flow of momentum through the system, again described in this chapter. By stepping beyond the limitations of the rocket equation, propellantless propulsion has the potential to enable new and exciting possibilities for the future which are currently impossible for conventional reaction propulsion devices.

7.2 Solar sailing

7.2.1 Introduction

The concept of solar sailing can be traced to various authors, including the Russian pioneers Tsiolkovsky [1] and Tsander [2]. However, serious development had to wait until a major NASA/JPL study during the mid-1970s for a proposed rendezvous mission to comet Halley [3]. Although being finally approved for flight, the study sparked international interest in solar sailing for future mission applications. It is only in recent years that sustained efforts have been made to develop the component technologies (reflective thin films and deployable booms) and to integrate these into a practical solar sail assembly. Development programmes are underway at both NASA and ESA to develop solar sail
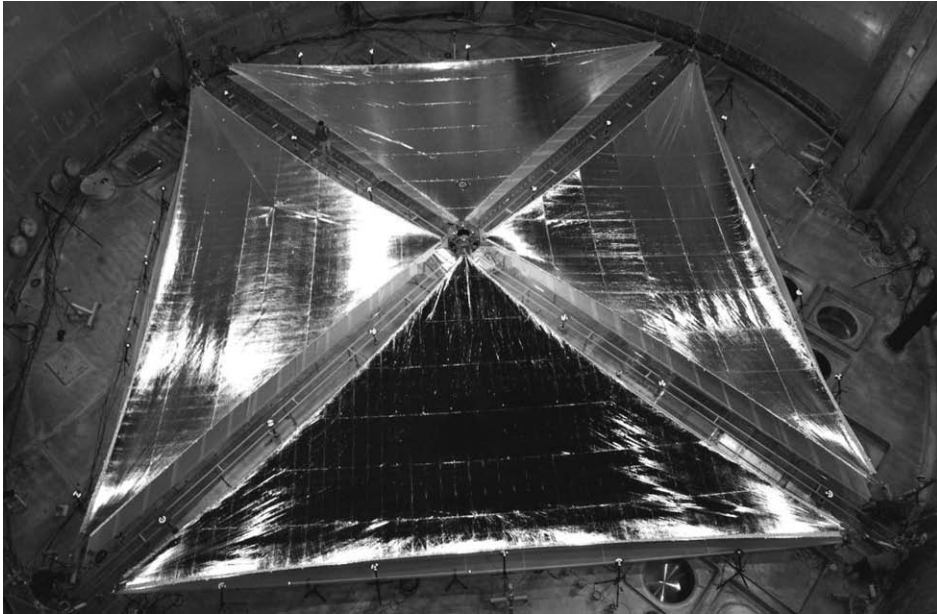
Fig. 7.1. NASA ground test of a $20 \times 20\,\text{m}$ solar sail (NASA/ATK).

technology through to flight status using ground testing and ultimately in-orbit demonstration missions (Figure 7.1). Should such demonstration missions prove successful, there are a wide range of potential mission applications which will then be enabled. The key missions on such a development roadmap are the Geosail mission, which uses a small solar sail to artificially precess a long elliptical orbit to maintain a space physics payload within the Earth's geomagnetic tail [4]; Geostorm, a space weather mission located sunward of the classical Sun–Earth L_1 point [5]; Polar Observer, a mission to station an imaging payload at an artificial equilibrium point high above L_1 [6]; Solar Polar Orbiter (SPO), a solar physics payload delivered to a close polar orbit about the Sun [7]; Interstellar Heliopause Probe (IHP), a small payload delivered to the heliopause at 200 AU in 25 years using a high performance solar sail [8]. In addition, solar sailing appears ideally suited to high-energy and/or long duration missions such as Mercury sample return [9], comet nucleus sample return and multiple small body rendezvous missions [10], as well as more exotic mission applications [11].

7.2.2 Solar sail sizing

The fundamental measure of performance of a solar sail is its characteristic acceleration, defined as the light pressure-induced acceleration experienced by the solar sail while oriented normal to the Sun at a heliocentric distance of 1 AU [12]. The characteristic acceleration is a function of both the efficiency of the solar sail design and the mass

of the payload. At a distance of 1 AU the magnitude of the solar radiation pressure P exerted on a perfectly absorbing surface is $4.56 \times 10^{-6} \, \text{Nm}^{-2}$. Therefore, allowing for the reflection of photons (factor of 2) and the finite efficiency of the sail η, the characteristic acceleration a_o is defined by

$$a_o = \frac{2\eta P}{\sigma}, \quad \sigma_T = \frac{m_T}{A}, \tag{7.1}$$

where σ_T is the total solar sail loading, with m_T the total mass of the solar sail and its payload and A the sail area. The sail efficiency η (typically ~ 0.85) is a function of both the optical properties of the sail film and the sail shape due to billowing and wrinkling. The total mass of the solar sail will now be partitioned into two components, the sail film and structural mass m_S and the payload mass m_P. Therefore, the characteristic acceleration of the solar sail may now be written as

$$a_o = \frac{2\eta P}{\sigma_S + (m_P/A)}, \quad \sigma_S = \frac{m_S}{A}, \tag{7.2}$$

where σ_S is the mass per unit area of the sail assembly. This so-called sail assembly loading is a key technology parameter and is a measure of the thickness of the sail film and the efficiency of the solar sail structural and mechanical design. Low performance solar sail concepts center on the use of commercially available $7.5\,\mu\text{m}$ Kapton film with a projected a sail assembly loading of order $30\,\text{gm}^{-2}$, which is adequate for near term technology demonstration missions. Other development work to fabricate ultra-thin sail films with a thickness of order $2\,\mu\text{m}$, and high stiffness, low mass booms is leading to a sail assembly loading of order $5\,\text{gm}^{-2}$ [13], or even as low as $1–2\,\text{gm}^{-2}$ for high performance spinning disk sails [14].

Now that the key solar sail design parameters have been defined, the process of sizing a solar sail will be considered. From Eq. (7.2) it can be seen that the solar sail payload mass may be written as

$$m_p = \left[\frac{2\eta P}{a_o} - \sigma_S\right] A. \tag{7.3}$$

Similarly, from Eq. (7.1) the total mass of the solar sail may be written as

$$m_T = \frac{2\eta PA}{a_o} \tag{7.4}$$

For a required characteristic acceleration, Eqs. (7.3) and (7.4) may now be used to size a solar sail while imposing constraints on the total mass of the solar sail to satisfy the capacity of the launch vehicle. A typical design space is shown in Figure 7.2 for a characteristic acceleration of $0.25\,\text{mms}^{-2}$, which is representative of the level of performance required for science missions such as a Mercury sample return. Both the payload mass and the total launch mass are shown. It is clear that for a payload of order $500\,\text{kg}$ and a sail assembly loading of order $5\,\text{gm}^{-2}$, a large sail is required with a sail side longer than $100\,\text{m}$. This requirement clearly poses challenges for the reliable mechanical deployment of large, low mass structures and the fabrication, packing and deployment of thin reflective films.
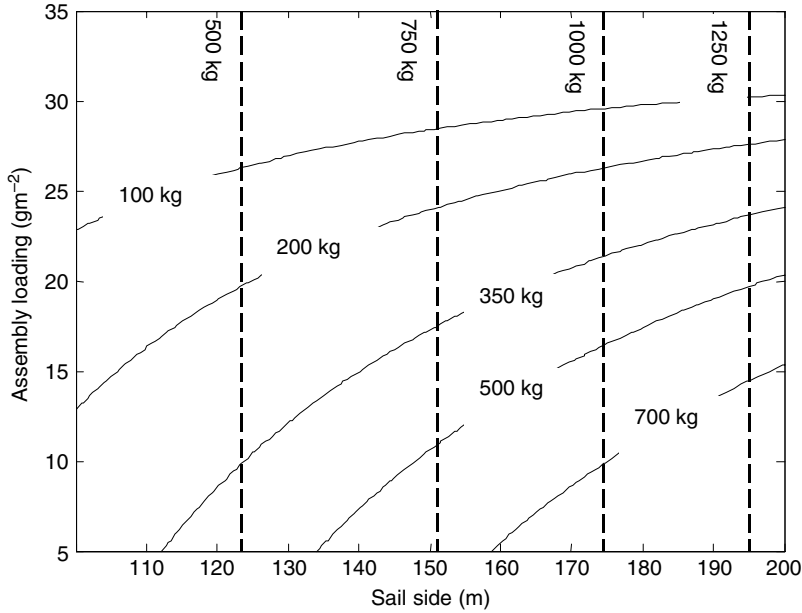
Fig. 7.2. Solar sail design space (solid line: payload mass, dashed line: total mass).

In addition to the design parameters discussed above, an additional parameter of interest can be defined. The payload mass fraction κ, defined by m_p/m_T can be obtained from Eqs. (7.3) and (7.4) as

$$\kappa = 1 - \frac{a_o \sigma_S}{2\eta P} \tag{7.5}$$

This is clearly another key parameter and is a measure of the efficiency of use of the solar sail. For a sail with a characteristic acceleration of $0.25\,\mathrm{mms^{-2}}$, which is again representative of the level of performance required for initial science missions, and a sail assembly loading of order $5\,\mathrm{gm^{-2}}$, the resulting payload mass fraction for the solar sail is 0.84, assuming an efficiency η of 0.85. It can be seen that improvements in sail assembly loading can either be used to increase the sail characteristic acceleration, and so reduce trip times, or can be used to improve the sail payload mass fraction, allowing a larger payload to be delivered for a fixed launch mass.

7.2.3 *Solar sail performance*

Since solar sails do not expel reaction mass, the conventional definition of specific impulse is inappropriate. This conventional definition relates the change in momentum of the spacecraft to the weight of propellant expelled. Since solar sails do not expel propellant they have, in principle, infinite specific impulse. However, for a finite mission duration, only a finite total impulse will be delivered by the solar sail. Infinite specific impulse is

only available for infinite mission duration. In order to circumvent this difficulty with the conventional definition of specific impulse, an effective specific impulse [15] will be defined as the total impulse delivered per unit weight of propulsion system

$$I_{sp} = \frac{1}{W} \int_0^T F \, \mathrm{d}t, \tag{7.6}$$

where F is the thrust delivered for mission duration T and W is the weight of the propulsion system. For a solar sail of total mass m_T and characteristic acceleration a_o at solar distance R (AU), the sail thrust is given by

$$F = m_T a_o \cos^2 \alpha \frac{1}{R^2}, \tag{7.7}$$

where α is the pitch angle of the sail normal relative to the Sun-sail line. The weight of the propulsion system will now be defined as the weight of the sail assembly so that for a sail assembly of mass m_S

$$W = m_s g_o. \tag{7.8}$$

The weight of the sail assembly can be then written in a more useful form as

$$m_S = m_T (1 - \kappa), \tag{7.9}$$

where κ is the payload mass fraction of the solar sail, defined by Eq. (7.5). Therefore, the effective specific impulse of the solar sail can now be written as

$$I_{sp} = \frac{1}{1 - \kappa} \frac{a_o}{g_o} T \left\langle \frac{\cos^2 a}{R^2} \right\rangle, \tag{7.10}$$

where $<>$ indicates the mean value over mission duration T. It can be seen that the effective specific impulse of the solar sail increases linearly with mission duration and as the inverse square of mean solar distance. In addition, $I_{sp} \to \infty$ as $\kappa \to 1$ since the weight of the propulsion system vanishes in this limit.

For a solar sail to be effective it can be seen that it must have a large payload mass fraction, and be used for a long duration. Missions such as high-energy comet sample returns will therefore make significantly better use of solar sails than, for example, payload delivery to the Moon or Mars where the effective ΔV is low (unless multiple trips are considered). In addition, inner solar system missions where R is small, such as Mercury sample return, will also make effective use of solar sailing. Deep space missions can also be effective, but a close pass to the Sun is required. This can be seen from Eq. (7.10) and is also evident from trajectory optimisation studies where the sail passes close to the Sun before being accelerated to some cruise speed for deep space payload delivery [8]. Earth escape also makes efficient use of solar sailing, although escape times can be long [16].

The effective specific impulse for a range of solar sails is shown in Figure 7.3, where it is assumed that the mean pitch angle α is 35° to maximise the transverse thrust, and the payload mass fraction κ is 2/3. It is clear that even if the sail has a low characteristic acceleration, it can deliver an extremely large effective specific impulse if the mission duration is long. This is exactly the relationship which makes the mission applications of the artificial Lagrange points discussed later in Sections 7.4 and 7.5 so attractive.
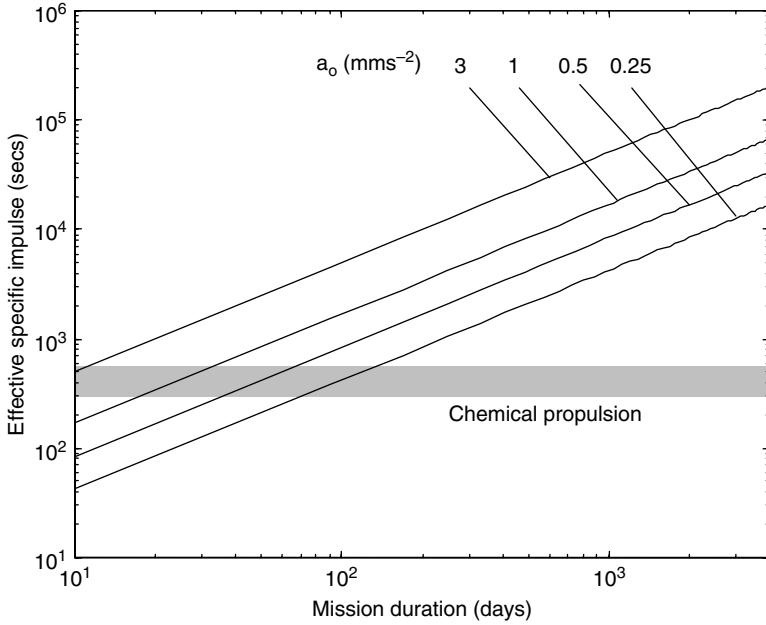
Fig. 7.3. Effective solar sail specific impulse.

7.3 Solar sail orbital mechanics

7.3.1 Introduction

The ratio of the solar radiation pressure force to the solar gravitational force exerted on the sail is defined by the sail lightness number β. Since both solar radiation pressure and solar gravity have an inverse square variation with solar distance, the sail lightness number is a constant for a given sail mass and area. It can be shown by considering the ratio of radiation pressure to gravitational forces that the sail lightness number is related to the total solar sail loading by $\sigma_T (gm^{-2}) = 1.53/\beta$, [12]. A high performance solar sail with a lightness number of 1 ($\sigma_T = 1.53\,\mathrm{gm}^{-2}$) corresponds to a characteristic acceleration of $5.96\,\mathrm{mms}^{-2}$. Such an advanced solar sail could exactly balance solar gravity, although near term solar sails are likely to have a characteristic acceleration of order $0.25\,\mathrm{mms}^{-2}$, as noted earlier.

An ideal, plane solar sail will now be considered moving relative to an inertial frame of reference with origin at the Sun. The vector equation of motion of the solar sail is then defined by

$$\frac{\mathrm{d}^2\mathbf{r}}{\mathrm{d}t^2} + \frac{\mu}{r^2}\hat{\mathbf{r}} = \beta\frac{\mu}{r^2}\left(\hat{\mathbf{r}}.\mathbf{n}\right)^2\mathbf{n}, \tag{7.11}$$

where $\mathbf{r}$ is the position vector of the spacecraft with respect to the Sun, with $\hat{\mathbf{r}}$ the associated unit vector. The product of the gravitational constant and the mass of the Sun

is defined by μ. For an ideal sail, the thrust vector is aligned along the sail unit normal **n**, with the sail pitch angle α, defined as the angle between the sail normal and the radius vector such that $\cos \alpha = \hat{\mathbf{r}}.\mathbf{n}$.

7.3.2 Conic section orbits

When the sail normal is directed along the Sun-line, such that $\mathbf{n} = \hat{\mathbf{r}}$, families of conic section orbits are obtained with a modified gravitational parameter, $\tilde{\mu} = \mu\,(1-\beta)$, since again solar gravity and solar radiation pressure both vary as the inverse square of the solar distance. For a lightness number $\beta = 0$, a circular Keplerian orbit will be assumed. Then, with $\beta \neq 0$ such an orbit becomes elliptical for $0 \prec \beta \prec 1/2$. With a lightness number $\beta = 1/2$ there is a transition from an elliptical orbit to a hyperbolic orbit through a parabolic orbit, which defines the lightness number necessary for direct escape. When the lightness number increases such that $1/2 \prec \beta \prec 1$, a hyperbolic orbit is obtained. Then, when the lightness number is exactly unity, there is the interesting situation where solar gravity is exactly balanced by solar radiation pressure. This could enable rectilinear orbits or could allow the solar sail to levitate, stationary relative to the Sun. With extremely high performance solar sails exhibiting lightness numbers of greater than unity, the Sun now becomes placed at the opposite focus of an (inverted) hyperbolic orbit since the solar radiation pressure force exceeds the solar gravitational force acting on the solar sail [17].

7.3.3 Logarithmic spiral trajectories

When the solar sail thrust is orientated at a fixed, non-zero pitch angle to the Sun-sail line it can be shown that the solar sail can follow a logarithmic spiral trajectory [18–20]. The radial component of the sail thrust reduces the effective gravitational force on the sail, however the component of thrust in the transverse direction acts to increase (or decrease) the orbital angular momentum of the solar sail. For a logarithmic spiral trajectory, the local solar sail speed is always less than the local circular orbit speed. This means that coplanar transfer by logarithmic spiral, between two circular orbits, cannot be achieved without hyperbolic excess at launch to place the solar sail onto the logarithmic spiral, and then an impulse to circularise the orbit on arrival at the final circular orbit. These discontinuities in the boundary conditions pose problems in the practical application of logarithmic spirals to orbit transfers.

7.3.4 Minimum-time trajectories

For practical mission analysis purposes, optimization is required to minimize the transfer time between any two orbits. Since the sail attitude will be time varying, the boundary conditions required for the transfer may be met without the use of initial and final

impulses, as required for the logarithmic spiral trajectory. First, the vector equation of motion will be re-cast as two, first order equations as

$$\dot{\mathbf{r}} = \mathbf{v} \tag{7.12a}$$

$$\dot{\mathbf{v}} = -\frac{\mu}{r^2}\hat{\mathbf{r}} + \beta\frac{\mu}{r^2}(\hat{\mathbf{r}}.\mathbf{n})^2\,\mathbf{n} \tag{7.12b}$$

with boundary conditions imposed on the solar sail trajectory such that the solar sail state is defined by $(\mathbf{r}_o, \mathbf{v}_o)$ at initial time t_o and $(\mathbf{r}_f, \mathbf{v}_f)$ at final time t_f, where $t_f = t_o + T$. The goal is now to minimize the transfer time T subject to the constraints imposed by the boundary conditions of the transfer. To proceed with the optimization process the control Hamiltonian function for the problem is formed. To ensure optimization, the Hamiltonian must be maximized at all points along the trajectory through an appropriate choice of sail attitude $\mathbf{n}$. The control Hamiltonian H is defined as

$$H = \mathbf{p}_r.\mathbf{v} - \frac{\mu}{r^2}\mathbf{p}_\nu.\hat{\mathbf{r}} + \beta\frac{\mu}{r^2}(\hat{\mathbf{r}}.\mathbf{n})^2\,\mathbf{p}_\nu.\mathbf{n}, \tag{7.13}$$

where $\mathbf{p}_r$ and $\mathbf{p}_\nu$ are the co-states for position and velocity [21]. The velocity co-state is also referred to as the primer vector and defines the direction along which the solar sail thrust should be maximized. Note that unlike other low thrust transfer problems there is no co-state for the solar sail mass since it is clearly constant. The rate of change of the co-states is then obtained from the control Hamiltonian as

$$\dot{\mathbf{p}}_r = -\frac{\partial H}{\partial \mathbf{r}} \tag{7.14a}$$

$$\dot{\mathbf{p}}_\nu = -\frac{\partial H}{\partial \mathbf{v}} \tag{7.14b}$$

so that

$$\dot{\mathbf{p}}_r = \frac{\mu}{r^3}\mathbf{p}_\nu - \frac{3\mu}{r^5}(\mathbf{p}_r.\mathbf{r})\,\mathbf{r} + 2\beta\frac{\mu}{r^3}(\hat{\mathbf{r}}.\mathbf{n})(\mathbf{p}_\nu.\mathbf{n})(\mathbf{n} + 2(\hat{\mathbf{r}}.\mathbf{n})\hat{\mathbf{r}}) \tag{7.15a}$$

$$\dot{\mathbf{p}}_\nu = -\mathbf{p}_r. \tag{7.15b}$$

The sail attitude $\mathbf{n}$ which maximises the Hamiltonian can then be found from Eq. (7.13) as a function of the co-states $\mathbf{p}_r$ and $\mathbf{p}_\nu$. The equations of motion must therefore be integrated along with the co-state equations, and an iterative numerical algorithm used to determine the initial co-states that provide a minimum-time trajectory that satisfies the boundary conditions of the transfer. An example minimum-time trajectory from Earth to Mercury is shown in Figure 7.4. As an alternative to the indirect approach of optimal control theory, direct methods can be used [10]. These algorithms discretize the sail attitude time history and minimize the transfer time using methods such as sequential quadratic programming. While direct methods are not as accurate as indirect methods, due to the discretization of the sail attitude, they can be more robust and flexible. Novel evolutionary algorithms have also been recently applied to the solar sail trajectory optimization problem [22], as have minimum-time transfers to 1 year Earth synchronous circular orbits [23].
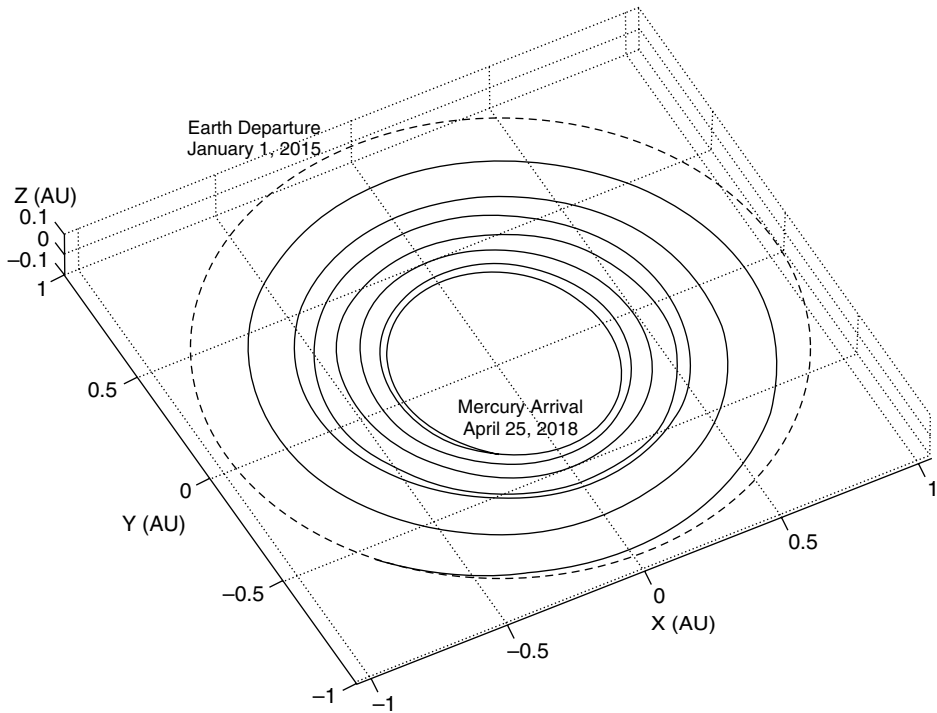
Earth Departure
January 1, 2015

Z (AU)
0.1
0
−0.1
1

0.5

0

Y (AU)

−0.5

−1 −1

Mercury Arrival
April 25, 2018

1

0.5

0

X (AU)

−0.5

Fig. 7.4. Minimum-time spiral from Earth to Mercury ($a_\mathrm{o} = 0.25\,\mathrm{mms^{-2}}$).

7.4 Artificial three-body equilibria for solar sails

7.4.1 Non-Keplerian orbits

Due to the continually available thrust from solar radiation pressure, solar sails are capable of exotic, highly non-Keplerian orbits. Although some of these orbits require advanced, high performance solar sails, others are possible using relatively modest solar sails. The solar sail performance required for these orbits is a function of the local gravitational acceleration. Therefore, to displace an orbit high above the plane of the solar system requires an extremely high characteristic acceleration, while to generate an artificial Lagrange point near the Earth may only require a near-term solar sail. While these highly non-Keplerian orbits are not, in principle, forbidden for other forms of low-thrust propulsion, they can only be achieved for a limited duration, fixed by the propellant mass fraction of the spacecraft. However, a solar sail stationed at an artificial Lagrange point and requiring a low-characteristic acceleration can still deliver an extremely high effective specific impulse if the sail film is long-lived and so used for an extended duration, as discussed in Section 7.2.2.

Using an advanced solar sail it would be possible to choose its characteristic acceleration so that the solar radiation pressure force exactly balances the local solar gravitational force,

corresponding to a lightness number β of 1. This is possible since, again, both of these forces have an inverse square variation with solar distance. The required characteristic acceleration for such a force balance is of order $6\,\mathrm{mms^{-2}}$, corresponding to a mass per unit area of only $1.5\,\mathrm{gm^{-2}}$, as discussed in Section 7.3.1. Such a high performance solar sail would enable solar physics missions which levitate above the solar poles, providing continuous observations, or indeed hover at any particular location in the solar system. Such a solar sail could also be used to displace circular Sun-centred orbits high above the plane of the solar system, with the orbit period chosen to be synchronous with the Earth or some other solar system body. Possible applications include stationing an infra-red telescope above the obscuring zodiacal dust within the ecliptic plane.

Using a more modest solar sail, the location of the Sun–Earth Lagrange points can be artificially displaced. For example, the interior L_1 point, 1.5 million km sunward of the Earth, is a favored location for solar physics missions. Since the solar sail adds an extra force to the dynamics of the problem the location of the L_1 point can be artificially displaced, closer to the Sun or even above the ecliptic plane. Since the local gravitational acceleration in the vicinity of L_1 is small (since centripetal force, solar and Earth gravity almost balance), only modest solar sails are required to provide a significant displacement of the classical L_1 point. For example, a solar sail with a characteristic acceleration of $0.25\,\mathrm{mms^{-2}}$ can double the distance of the L_1 point form the Earth. Such a new sunward equilibrium location appears useful for providing early warning of disruptive solar plasma storms before they reach Earth, an indeed formed the basis for the Geostorm mission concept, discussed later in Section 7.5.1. A solar sail with double the performance can be permanently stationed high above (or below) the classical L_1 point so that it appears above the Arctic (or Antarctic) regions of the Earth, again to be discussed later in Section 7.5.2.

7.4.2 *Artificial three-body equilibria: ideal solar sail*

This section will investigate the possibility of artificial Lagrange points for near-term, low performance solar sails [24–27]. Equilibrium solutions will be obtained for an ideal solar sail and then the problem will be re-visited with a more realistic partially reflecting solar sail. Apart from reducing the magnitude of the radiation pressure force exerted on the solar sail, the finite absorption of a realistic sail means that the radiation pressure force vector is no longer directed normal to the sail surface. Due to this effect, it will be shown that the volume of space available for artificial Lagrange points is extremely sensitive to the solar sail reflectivity.

Equilibrium solutions for an idealized, perfectly reflecting solar sail will now be derived. The ideal sail will be considered in a frame of reference co-rotating with two primary masses m_1 (Sun) and m_2 (Earth) at constant angular velocity $\boldsymbol{\omega}$, as shown in Figure 7.5. The sail attitude is again defined by a unit vector $\mathbf{n}$ normal to the sail surface, fixed in the rotating frame of reference. The units of the problem will be chosen such that the gravitational constant, the distance between the two primary masses and their sum are all taken to be unity.
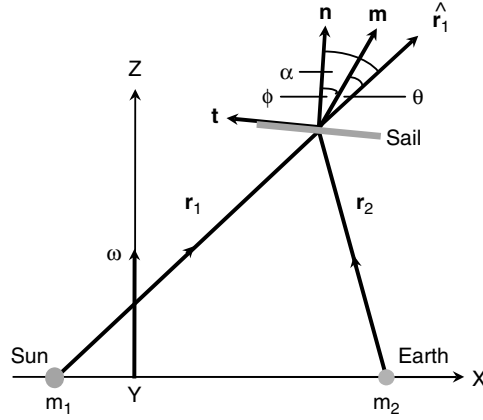
Fig. 7.5. Sun–Earth restricted three-body problem with a partially reflecting solar sail.

The vector equation of motion for a solar sail in this rotating frame of reference may then be written as

$$\frac{d^2\mathbf{r}}{dt^2} + 2\boldsymbol{\omega} \times \frac{d\mathbf{r}}{dt} + \nabla U = \mathbf{a} \tag{7.16}$$

with the three-body gravitational potential U and the solar radiation pressure acceleration $\mathbf{a}$ defined by

$$U = -\left[\frac{1}{2}(x^2 + y^2) + \frac{1-\mu}{r_1} + \frac{\mu}{r_2} \right], \tag{7.17a}$$

$$\mathbf{a} = \beta \frac{1-\mu}{r_1^2} (\hat{\mathbf{r}}_1.\mathbf{n})^2 \mathbf{n}, \tag{7.17b}$$

where $\mu = m_1 / (m_1 + m_2)$ is the mass ratio of the system and the sail position vectors are defined as $\mathbf{r}_1 = (x + \mu, y, z)$ and $\mathbf{r}_2 = (x - (1 - \mu), y, z)$.

Equilibrium solutions are now required in the rotating frame of reference so that the first two terms of Eq. (7.16) vanish. The five classical Lagrange points are then obtained as the solutions to $\nabla U = 0$ with $\hat{\mathbf{r}}_1.\mathbf{n} = 0$ and so $\mathbf{a} = 0$. However, for $\hat{\mathbf{r}}_1.\mathbf{n} > 0$ there is an additional acceleration $\mathbf{a}$ which is a function of the lightness number β and the sail attitude $\mathbf{n}$ so that new artificial equilibrium solutions may be generated. Since the vector $\mathbf{a}$ is oriented in direction $\mathbf{n}$, taking the vector product of $\mathbf{n}$ with Eq. (7.16) it follows that

$$\nabla U \times \mathbf{n} = 0 \Rightarrow \mathbf{n} = \lambda \nabla U, \tag{7.18}$$

where λ is an arbitrary scalar multiplier. Using the normalization condition $|\mathbf{n}| = 1$, λ is identified as $|\nabla U|^{-1}$ so that the required sail attitude is defined by

$$\mathbf{n} = \frac{\nabla U}{|\nabla U|} \tag{7.19}$$

which can be used to obtain the sail pitch angle α, since $\cos \alpha = \hat{\mathbf{r}}.\mathbf{n}$. The required sail lightness number may also be obtained by taking a scalar product of Eq. (7.16) with $\mathbf{n}$. Again requiring an equilibrium solution it is found that

$$\beta = \frac{r_1^2}{(1-\mu)} \frac{\nabla U.\mathbf{n}}{(\hat{\mathbf{r}}_1.\mathbf{n})^2} \tag{7.20}$$

Since the sail lightness number and attitude can be selected, the set of five classical Lagrange points will be replaced by an infinite set of artificially generated equilibrium solutions. These solutions form enclosed, nested surfaces, parameterized by the sail lightness number β.

The regions in which these new solutions may exist are defined by the constraint $\hat{\mathbf{r}}_1.\nabla U \geq 0$ with a boundary surface defined by an equality. This constraint may be understood physically since the solar radiation pressure acceleration vector $\mathbf{a}$, and so the sail attitude vector $\mathbf{n}$, can never be directed sunward. The boundary surface has two topologically disconnected surfaces S_1 and S_2 which define the region of existence of equilibrium solutions near m_2, as shown in Figure 7.6. The classical equilibrium solutions lie on either S_1 or S_2 since they are the solutions to $\nabla U = 0$. Surfaces of constant sail lightness number generated from Eq. (7.20) for the Earth–Sun system are also shown in Figure 7.6. In general, the surfaces of constant sail lightness number approach these
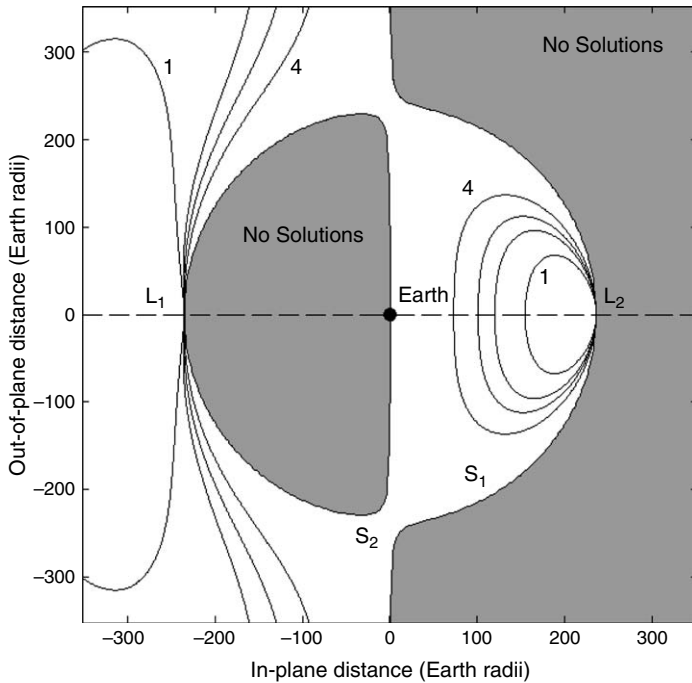

Fig. 7.6. Contours of sail loading in the *x–z* plan with reflectivity $\eta = 1$. Contours (gm^{-2}): [1] 30 [2] 15 [3] 10 [4] 5.

boundaries asymptotically with $\beta \to \infty$ when $\hat{\mathbf{r}}_1.\nabla U \to 0$, as is clear from Eq. (7.20). It can be seen that as the sail lightness number increases larger volumes of space are accessible for artificial equilibrium points. In particular, a solar sail of a given lightness number can be in equilibrium sunward or above/below the classical L_1 and L_2 points. In addition, in the limit $\mu \to 0$, displaced two-body orbits are obtained whose orbit period can be selected by an appropriate choice of sail lightness number and sail pitch angle [17].

7.4.3 Artificial three-body equilibria: realistic solar sail

A realistic solar sail force model which includes absorption will now be considered. To allow a closed-form solution, the solar sail will be assumed to have perfect specular reflectivity and no thermal re-emission but will still have an overall reflectivity η less than unity. Then, the radiation pressure acceleration will act in direction $\mathbf{m}$ and may be written as the sum of components normal $\mathbf{n}$ and transverse $\mathbf{t}$ to the sail surface such that

$$a\mathbf{m} = \frac{1}{2}\beta \frac{1-\mu}{r_1^2}(1+\eta)(\hat{\mathbf{r}}_1.\mathbf{n})^2\mathbf{n} + \frac{1}{2}\beta\frac{1-\mu}{r_1^2}(1-\eta)(\hat{\mathbf{r}}_1.\mathbf{n})(\hat{\mathbf{r}}_1.\mathbf{t})\mathbf{t}. \qquad (7.21)$$

It can be seen that the main effect of the non-perfect reflectivity of the sail is to reduce the acceleration magnitude and to introduce an off-set in the direction of the radiation pressure acceleration. The acceleration $\mathbf{a}$ now acts in direction $\mathbf{m}$ rather than normal to the sail surface in direction $\mathbf{n}$. This off-set is defined by the centre-line angle ϕ, with the actual radiation pressure force direction defined by a cone angle θ, as shown in Figure 7.5.

The analysis presented in the previous Section will be repeated using the sail force model defined by Eq. (7.21) so that the equation of motion may now be written as

$$\frac{d^2\mathbf{r}}{dt^2} + 2\boldsymbol{\omega} \times \frac{d\mathbf{r}}{dt} + \nabla U = a\mathbf{m}. \qquad (7.22)$$

For an equilibrium solution the first two terms of Eq. (7.22) will again vanish so that the sail attitude must be chosen as

$$\mathbf{m} = \frac{\nabla U}{|\nabla U|}. \qquad (7.23)$$

The unit vector $\mathbf{m}$ can now be defined by the cone angle θ between the radial direction $\hat{\mathbf{r}}_1$ and $\mathbf{m}$ as

$$\tan \theta = \frac{|\hat{\mathbf{r}}_1 \times \nabla U|}{\hat{\mathbf{r}}_1.\nabla U}. \qquad (7.24)$$

In addition, using Eq. (7.21) the centre-line angle can be obtained from the ratio of the transverse and normal accelerations as

$$\tan \phi = \frac{1-\eta}{1+\eta}\tan \alpha, \qquad (7.25)$$

where the sail pitch angle $\alpha = \theta + \phi$. Noting that $\mathbf{n.t} = 0$ and taking a scalar product of Eq. (7.22) with the unit vector $\mathbf{n}$ gives the required sail lightness number as

$$\beta = \frac{2r_1^2}{1-\mu} \frac{\nabla U.\mathbf{n}}{(1+\eta)(\hat{\mathbf{r}}_1.\mathbf{n})^2} \qquad (7.26)$$

The center-line angle may be obtained explicitly by again noting that $\alpha = \theta + \phi$. Then, after some reduction, Eq. (7.25) yields the center-line angle directly from the cone angle as

$$\tan \phi = \frac{\eta}{(1+\eta)\tan \theta} \left[1 - \left[1 - \frac{1-\eta^2}{\eta^2} \tan^2 \theta \right]^{1/2} \right] \qquad (7.27)$$

Lastly, using Eq. (7.26) it is found that the required sail lightness number may be obtained in terms of the lightness number for an ideal solar sail $\tilde{\beta}$ as

$$\beta = \frac{2}{(1+\eta)} \frac{\sqrt{1+\tan^2 \phi}}{(1-\tan \theta \tan \phi)^2} \tilde{\beta} \qquad (7.28)$$

where $\tilde{\beta}$ is defined by Eq. (7.20). Therefore, using Eqs. (7.24), (7.27) and (7.20) the sail orientation and sail lightness number required for an artificial equilibrium solution can be obtained.

The effect of a non-ideal solar sail is shown in Figure 7.7 for a reflectivity of 0.9, typical of a flat aluminized sail film. First, it can be seen that the volume of space available for equilibrium solutions about L_2 is significantly reduced. This is due to the center-line angle which limits the direction in which the radiation pressure force vector can be oriented. For solutions near L_1 the main effect of the non-ideal sail is to displace the equilibrium solutions towards the Earth. This is due to the reduction in the magnitude of the radiation pressure force, rather than the center-line angle. In general then, equilibrium solutions sunward of L_1 are not greatly affected by a realistic sail while equilibrium solutions about L_2 are severely restricted.

7.5 Mission applications

7.5.1 Geostorm mission

Currently, warnings of geomagnetic storms are made using terrestrial data and real-time solar wind data obtained from the Advanced Composition Explorer (ACE) spacecraft, stationed on a halo orbit [28] about the L_1 Lagrange point some 1.5 million km (0.01 AU) sunward of the Earth, as shown in Figure 7.8. Since the spacecraft is located sunward of the Earth, coronal mass ejections (CME) sensed by the suite of instruments on-board the ACE spacecraft can be used to provide early warning of impending geomagnetic storms. Typically, a prediction of 30–60 minutes can be made from the L_1 point, enhancing the quality of forecasts and alerts to operational user groups. These groups include civil and military satellite operators, electricity utility companies and airlines.
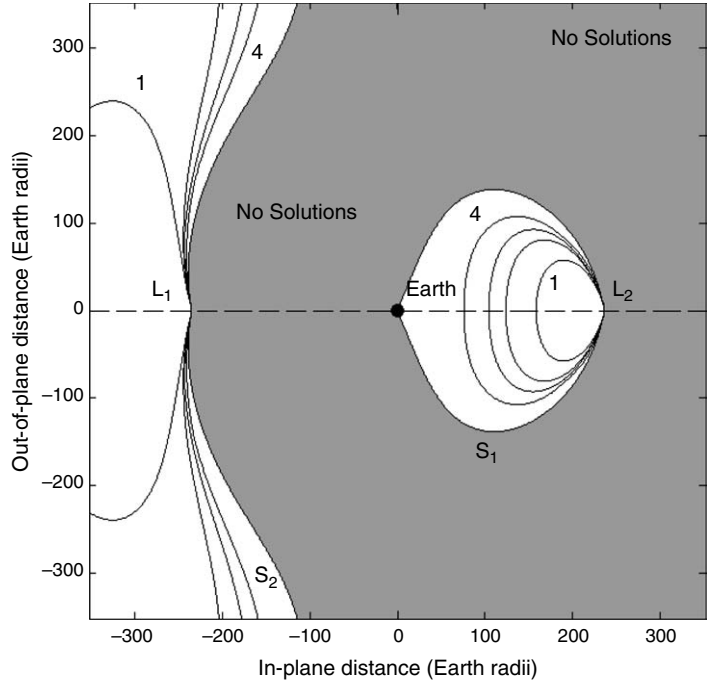
Fig. 7.7. Contours of sail loading in the x–z plan with reflectivity $\eta = 0.9$. Contours $(\mathrm{g\,m^{-2}})$: [1] 30 [2] 15 [3] 10 [4] 5.
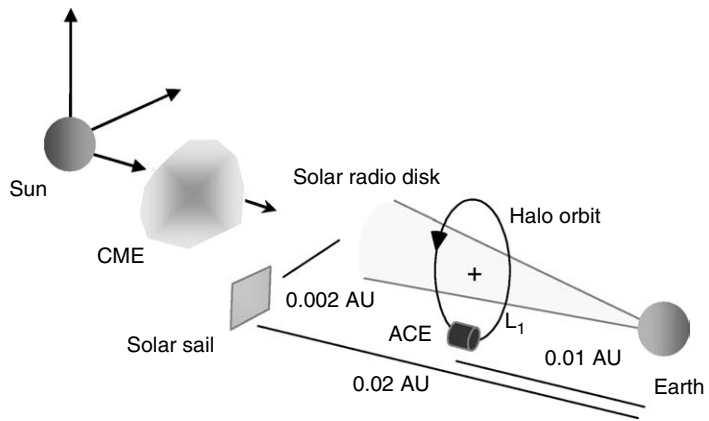

Fig. 7.8. Geostorm mission concept.

To enhance this warning time would require a spacecraft to be stationed at an artificial Lagrange point, sunward of the classical L_1 point, as discussed in Section 7.4. While this would require an unrealistic ΔV budget for a conventional spacecraft (of order $9\,\mathrm{km s}^{-1}$ per year of operation), a relatively small solar sail can be used to station a spacecraft approximately 3 million km (0.02 AU) from the Earth, again shown in Figure 7.8. This new artificial Lagrange point will double the warning time of impending geomagnetic storms [5]. The artificial Lagrange point must also be displaced away from the Sun–Earth line so that from the Earth, the spacecraft is viewed away from the solar radio disk to avoid interference with telemetry down-link. The volume of space accessible near L_1 in the ecliptic plane is shown in Figure 7.9, along with the Geostorm mission sub-L_1 design point. The Geostorm mission makes excellent use of solar sailing by only requiring a modest solar sail characteristic acceleration, but delivering an extremely high effective specific impulse for a multi-year mission duration, as discussed in Section 7.2.3. The solar sail can be transferred to the artificial Lagrange point by chemical kick-stages (and deployed on-station), or the solar sail can perform the transfer.
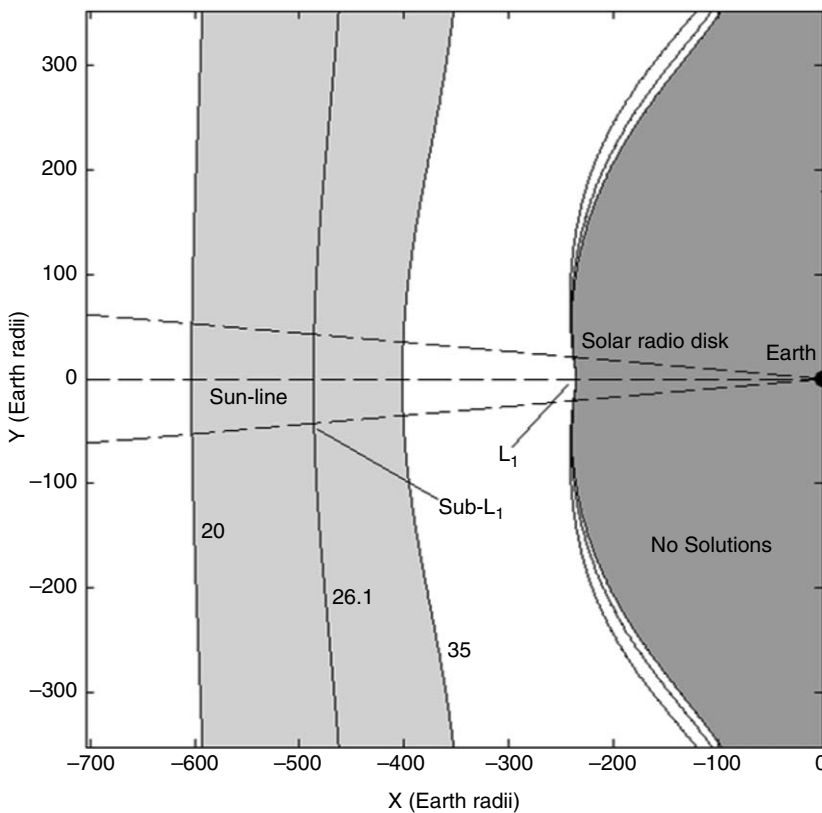

Fig. 7.9. Volume of space accessible in ecliptic plane for sail loadings 20–35 gm^{-2}.

7.5.2 *Polar observer mission*

It has been seen in Section 7.4 that solar sails may be used to generate artificial equilibrium solutions in the Sun–Earth three-body system. While in-plane equilibria have applications for missions such as Geostorm, out-of-plane equilibria may be utilised for continual, low-resolution imaging of the high latitude regions of the Earth. In fact, if the artificial Lagrange point is located high enough above or below the ecliptic plane, the solar sail may be stationed directly over the north pole, or indeed the south pole, during the summer solstice [24, 6]. The solar sail can be stationed directly over the north pole at the summer solstice, as shown in Figure 7.10, but will not remain over the pole during the entire year due to the tilt of the polar axis. From this unique vantage point a constant daylight view of the north pole is available at the summer solstice, however six months later at the winter solstice the polar regions are in permanent darkness. The volume of space accessible above L_1 is shown in Figure 7.11, along with the optimum Polar Observer mission design point. It is found that the required solar sail performance can be minimized by an appropriate selection of polar altitude. It can be shown that an equilibrium location some 3.8 million km (596 Earth radii) above the north pole will minimize demands on the solar sail performance. Closer equilibrium locations are possible using larger, or higher performance solar sails, or indeed selecting a less demanding viewing geometry.

Although the distance of the solar sail from the Earth is large for imaging purposes, there are potential applications for real-time, low-resolution images for continuous views of large scale polar weather systems along with Arctic ice and cloud coverage for
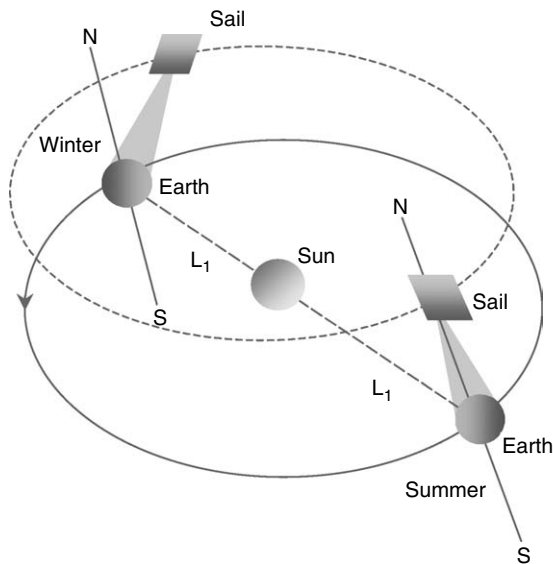

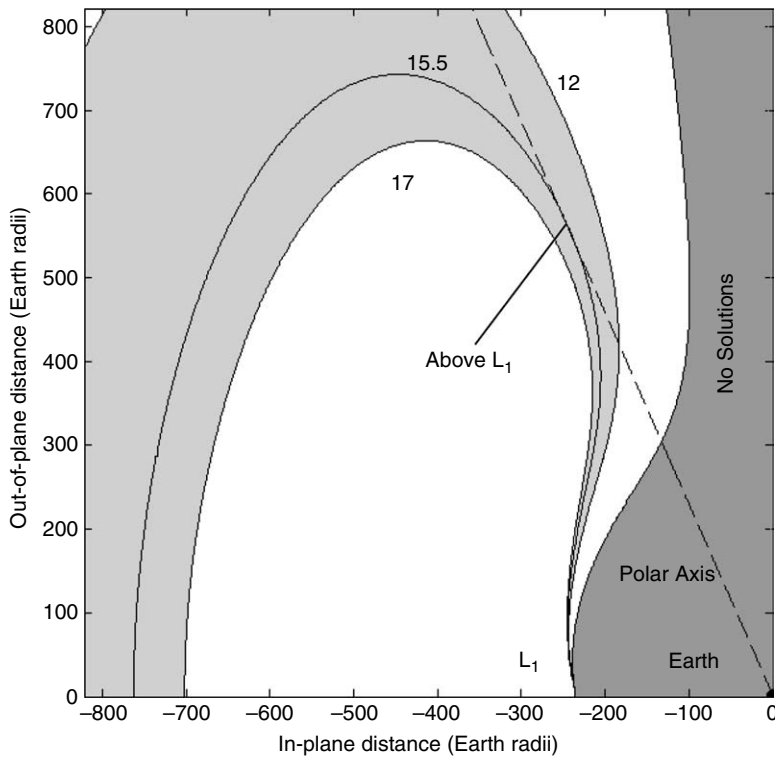Fig. 7.10. Polar Observer mission concept.

Fig. 7.11. Volume of space accessible out of ecliptic plane for sail loadings 12–17 gm^{-2}.

global climate studies. Although such images can be acquired by assembling a mosaic of instrument swaths from a conventional polar orbiting satellite, many high latitude passes are required to form a complete image. High resolution is then possible, but the completed image is not acquired in real-time and so dynamic phenomena cannot be captured.

For a 30 cm aperture instrument stationed 3.8 million km from the Earth and operating at optical wavelengths, a minimum ground resolution of order 10 km is possible, which is suitable for synoptic imaging. In practice though, the actual resolution obtained will be degraded due to factors such as the pointing stability of the camera. Higher resolution is possible if an equilibrium location closer to the pole is selected, at the expense of increased demands on the solar sail performance. Other applications of these orbits include line-of-sight, low-bandwidth communications to high-latitude users, such as Arctic or Antarctic stations. Applications for continuous data links to Mars polar landers and surface rovers have also been explored for a solar sail stationed high above the poles of Mars. Again, the Polar Observer mission makes excellent use of solar sailing by delivering an extremely high effective specific impulse for a multi-year mission duration.

7.6 Tethers in space

7.6.1 Introduction

The development of tether technology has had a strong international effort, with its origins over a century ago, and so only a limited selection of the many interesting concepts that have been proposed can be given here. The first serious reference to tether-like systems is usually attributed to Tsiolkovsky for proposals going back to 1895 [29] for a *space tower* linking a *celestial castle*, located at geostationary altitude and connected to a point on the surface of the Earth. The idea was based on an equatorial attachment point for the lower end of the tower which would be used for payload transfer into orbit and back to the Earth's surface. Now, as then, the construction of a tower tens of thousands of kilometres in length is beset with practical difficulties, despite major advances in modern materials science research. However the idea persisted and was taken up next by Artsutanov [30], who proposed the lowering of a cable from a geosynchronous satellite, with a suitable counterweight to be extended from the satellite into space to maintain tension in the system, and electric payload propulsion along the cable. The key problem of identifying commercially available material in realistic, and affordable quantities for the very high strength lightweight cable continued to be unsolved.

Roughly in parallel with this, Isaaks et al. [31] established the *Sky-hook* scenario in 1966, intended for the launch of payloads into space using the space elevator principle. The proposal was for an elevator to be deployed from the geostationary point in the form of two cables directed both towards the Earth and away from it. The cable design involved a taper in order to limit mass and to enhance strength as far as possible. The idea was based on harnessing the acceleration along the cable in order to generate payload lift from Earth, and so provide a purely mechanical launch capability for satellites and payloads into orbit. Identification of an appropriate material for the tapered cable still posed many challenges.

Applications of cables for payload movement received additional impetus in 1975 in the form of Grossi's original patented idea for a shuttle-borne orbiting *tether* [32] exploiting momentum exchange. Further work by Colombo, Grossi, and colleagues at the Smithsonian Astrophysical Laboratory has since been responsible for many major contributions to tether analysis and flights, several of which are summarized in the authoritative *Tethers in Space Handbook* [33]. Moravec [34] conceptualized the intriguing *Lunavator* tether proposal for surface payload collection and deposition on the Moon and other airless planets. This was based on a more generalized *rotovator* idea which enabled Moravec to show that limitations on current and future material strength, that would otherwise lead to an impractically high tether/payload mass for Earth surface contacts, would not necessarily impose the same restrictions for touch-downs on the Moon. The Lunavator concept has since been built into many tether mission concepts involving the Moon.

Although primary access to space using mechanical tethers is as practically challenging and potentially infeasible as it ever was, interest in tether systems has continued by moving towards rather less demanding, medium-term tether applications based on multi-strand polymeric tethers with small cable diameters and significant built-in redundancy.

The patented *Hoytether*^{TM} is a well known example of such a design [35]. Typical applications are momentum exchange tethers for propellant-less de-orbiting of satellites, and sample return or waste disposal using re-entry vehicles deployed from space platforms. In addition to momentum exchange the electrodynamic effects of a gravity gradient stabilised conductive tether system can also be applied, either for the generation of electrical power, or as means for orbit raising and lowering. Carroll proposed a simple deployment-only tether known as the Small Expendable Deployer System (SEDS) in 1983 and then published a generic and very useful guidebook for the analysis of the wide range of tether applications studied up to that time [36].

In the mid to late 1990s Cartmell [37] showed independently that dumb-bell tether models could benefit from additional energy injected by a centrally located drive motor. This proposal enhanced the potential performance of spinning momentum exchange tethers as long as a suitable counter-inertia could be contrived for the motor to work against. Symmetry can be exploited in the form of two identical payloads and for such a system orbiting about Earth it has been shown that the outer payload can be boosted, potentially for Lunar Transfer, whilst the inner payload is de-boosted for return to the Earth's surface [38–41]. Staged Motorised Momentum Exchange Tethers (MMETs) are theoretically capable of generating ΔVs of up to 2 km/s, or more using conventional materials, although considerable research remains to be done on practically feasible orbital mechanics and mission logistics [42].

Tether flight experiments commenced in the mid 1960s with the manned Gemini 11/Agena mission in which the Gemini vehicle was linked to the Agena target vehicle by means of a 30 m tether. The first attempts to use a long deployed tether in space were the Tethered Satellite System (TSS) missions in which gravity gradient stabilized conductive tether systems, emanating from the Shuttle and deploying a satellite, were to be used for investigations in space physics and plasma-electrodynamics [33]. TSS-1 was the first of these, in July 1992, and was intended to explore the use of a retrievable tether. The tether was a 20 km Kevlar/Nomex conductive tether containing ten strands of 34 AWG copper wire (34 AWG is slightly less than 0.25 mm) but due to a protruding bolt the tether only actually deployed to about 256 m. However, it still verified some fundamental dynamics issues concerned with short deployment and gravity gradient stabilization, with implications for longer deployments. This led on to TSS-1R in February 1996, which successfully deployed to 19.7 km, just slightly short of the 20.7 km that had been planned. Plasma phenomena were observed with the conductive tether used and showed that currents significantly in excess of numerical predictions could be collected [33].

The Small Expendable Deployer missions, SEDS-1 and SEDS-2, were flown in March 1993 and 1994 showing that a small test payload of 25 kg could be de-orbited from LEO, and also that a closed loop controller could be used to deploy a tethered payload along a limited angle with respect to the local vertical. The SEDS-2 mission deployed to 19.7 km, and utilized a friction multiplier brake during deployment, an interesting concept which is currently being incorporated in the form of a *barberpole* design within the forthcoming YES2 mission [43] and which was theoretically and experimentally investigated by Lennert and Cartmell [44]. This work, along with other theoretical and experimental studies [43], showed that the friction characteristics between practical tethers wrapped in a spiral around a metallic cylindrical surface can generate useful braking forces

involving significant speed-dependencies. There are some phenomenological analogies with literature observations in automotive disk-pad brake systems [45].

Dynamic analysis was one of the goals of the OEDIPUS-C flight in November 1995 in which two fore and aft payloads were used to implement and demonstrate spin stabilization by means of the so-called Tether Dynamics Experiment (TDE). The dynamics of spinning tethered two-body *dumb-bell* systems have received considerable literature attention and this experiment provided valuable in-service tether force data and payload nutation responses within the time domain. Another notable mission was the Tether Physics and Survivability Experiment (TiPS) in 1996 based on two end-bodies known as Ralph and Norton (after Ralph Kramden and Ed Norton, who starred in the 1950s comedy show *The Honeymooners*). Ralph and Norton were connected together by a 4 km insulating tether. Norton, at 10.8 kg, was mounted closest to the host vehicle and contained no electronics whereas Ralph, at 37.7 kg and at the other end, contained the electronics, instrumentation, and the tether deployer, as shown in Figure 7.12. The TiPS system was ejected from the host spacecraft in June 1996 and the objectives were to investigate long-term orbit and attitude dynamics and survivability. This successful flight provided data which suggested that reasonable long-term survivability could be expected and that predicted stabilizations of small angle libration are practically achievable [33]. Subsequent tether missions have been subject to various delays and cancellations (ATEx, ProSEDS, TSE, STEP-AirSEDS, and ASTOR, are notable examples), but at the time of writing the Young Engineers' Satellite 2 (YES2) sample return mission from the ISS is still under active technology development [43]. A major tether project which is also currently under intensive development is NASA's *Momentum Exchange Electrodynamic Reboost* (MXER) concept in which momentum exchange is to be used to transfer payloads from LEO to geosynchronous transfer orbit and beyond, after which electricity from solar panels fitted to the system would be used to drive current through the tether in order to re-boost the tether by means of an interaction against the geomagnetic field, thereby restoring the energy that was transferred to the payload [46].

7.6.2 Hanging, swinging, and spinning tethers

7.6.2.1 Hanging tethers

One of the fundamentals of space tether applications is that two tethered masses orbiting a source of gravity in space must possess the same orbital angular velocity as the overall centre of mass (CoM) [38]. Figure 7.13 shows the case of a hanging dumb-bell tether in which the upper payload (UP) is released from a hanging tether and then onto an elliptical orbit. This is because the upper payload carries more velocity than required for that orbit, but not enough to escape the influence of the Earth. The payload's release point is then the perigee of that elliptical orbit. On release of the upper payload the lower payload (LP) and the tether do not have enough velocity to stay on the original orbit so they also go into an elliptical orbit, but with the release point at the apogee. Half an orbit later the UP reaches its apogee, and so it is further away from the Earth than it was when it was released. Similarly the LP and the tether reach their perigee and are therefore closer to the Earth than they were when the UP was released. This means that the upper and lower payloads of a hanging tether are, respectively, raised and lowered.
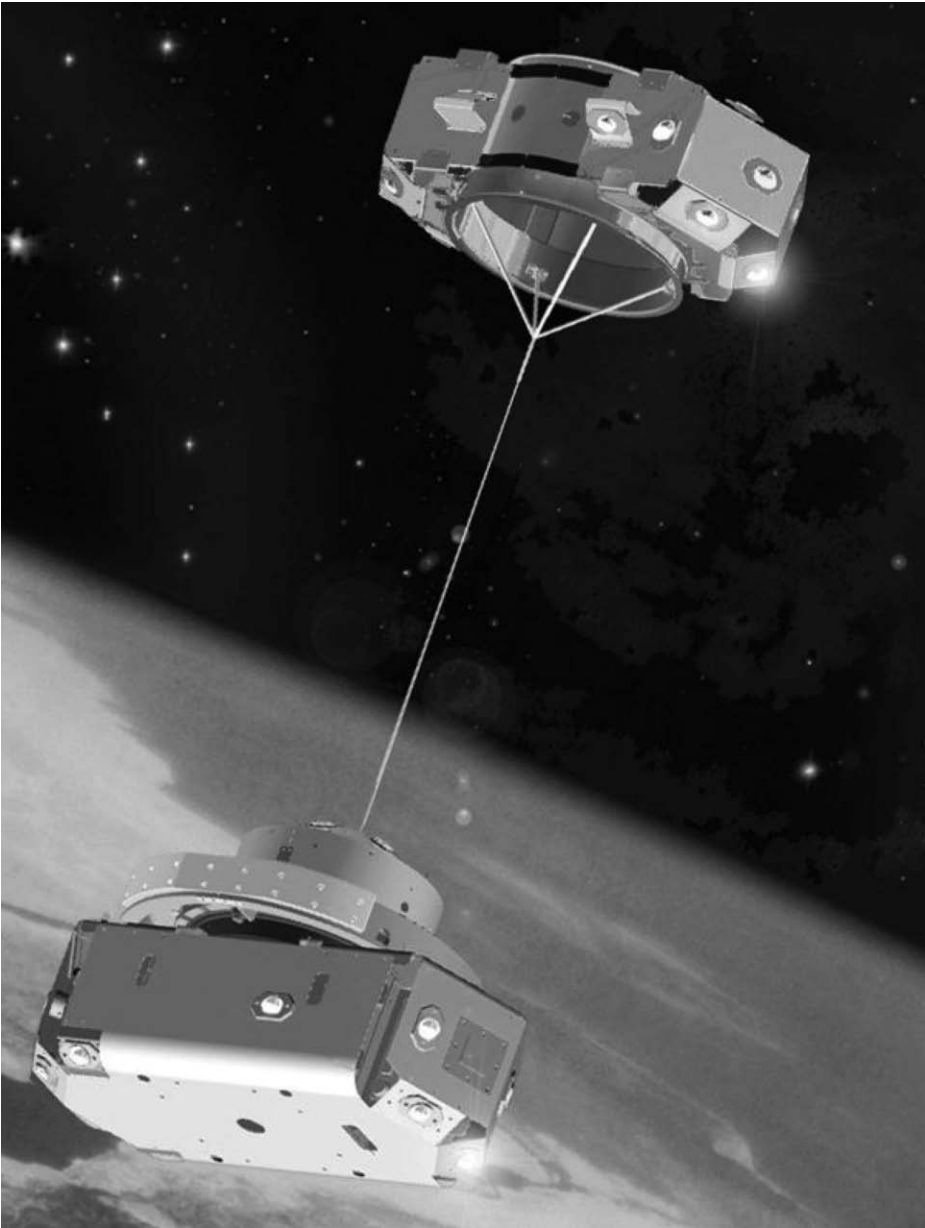
Fig. 7.12. Artist's rendition of TiPS tether in orbit configuration (Naval Research Laboratory).
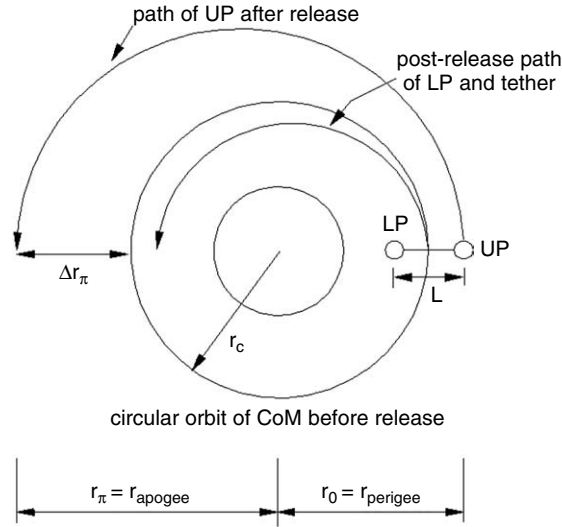
Fig. 7.13. Upper and lower payload separations and definition of Δr_π [38, 39].

7.6.2.2 *Adding swinging or spin motion*

A prograde swing or spin will add velocity to the upper payload and will subtract velocity from the lower payload. Conversely a retrograde swing or spin will subtract velocity from the UP and add velocity to the LP. So, retrograde swing or spin could be used to maintain the original orbit of the UP on release, for example. For maximum apogee altitude gain of the UP, and perigee altitude loss of the LP, the most desirable tether motion has to be either a prograde swing or spin. It appears that the optimum payload release point for a swinging or spinning tether is when it is aligned along the local gravity vector and when the motion is coplanar with the orbital plane [38]. The radial separation, Δr_π, between a payload half an orbit after release, and the tether CoM's circular orbital radius at release, is usually defined as being greater than the sub-span length l for orbit raising and less than l for orbit lowering (where the end-to-end length equals twice the sub-span, i.e., $L = 2l$).

7.6.2.3 *Literature applications and proposals*

The first well-known proposal for payload orbit raising or lowering using momentum exchange tethers was made by Colombo et al. [47]. Soon after that a system based on a hanging tether in a circular orbit was proposed by Bekey and Penzo [48], for payload transfer from LEO to Geostationary orbit. This also raised the problem of unwanted lowering (effectively de-orbiting) of the mass at the other end (in this case the shuttle) and also potential problems with excessive tether tension. Kelly [49] suggested that the shuttle could be tethered to its external fuel tank at separation in order to raise the shuttle's orbit and to de-orbit the tank. Lorenzini et al. [50] suggested propelling a payload from LEO to GEO using a two-stage tether system, with transfer times that were found to be

potentially comparable to those for a conventional chemically propelled upper stage. The tethers were shown to be better in terms of mass reduction.

7.6.2.4 Literature analyses and results

The commonly quoted literature result for an UP released from a hanging tether is that it rises approximately seven times its sub-span length half an orbit later, therefore,

$$\Delta r_\pi \approx 7l. \tag{7.29}$$

In the case of swinging and spinning tethers, respectively, it has been shown that,

$$\Delta r_\pi < 14l \tag{7.30}$$

$$\Delta r_\pi > 14l \tag{7.31}$$

[33, 48, 50–52]. Bekey [53], also claimed that Eq. (7.31) could be extended as far as,

$$\Delta r_\pi > 25l. \tag{7.32}$$

It was shown by Cosmo and Lorenzini [33] that the swing angle of a swinging tether could be incorporated into such expressions and they went on to show that a swinging tether could generate a Δr_π of,

$$\Delta r_\pi \approx (7 + \sqrt{48}\sin\theta_{\text{max}})l, \tag{7.33}$$

where θ_{max} was defined as the maximum swing angle attainable and considered to be positive for prograde motion and negative for retrograde motion. This analysis assumed that the tether and LP remained on their original circular orbit. According to Cosmo and Lorenzini [33] the equations above only hold for $\Delta r_\pi \ll r_c$. Finally, in this short summary, we note another expression, this time due to Kumar et al. [54] which holds for both swinging and spinning systems on the assumption that $l \ll r_c$, where here $\dot\theta$ and $\dot\Psi$ are the angular orbital and pitch velocities, both in rad/s,

$$\Delta r_\pi \approx \left(7 + 4\frac{\dot\Psi}{\dot\theta}\right)l. \tag{7.34}$$

One can readily see from this that although Eq. (7.33) is independent of both the orbital radius of the facility (central system) and the payload mass these quantities will clearly affect the momentum of the payload in practice. Similarly, although Eq. (7.34) takes the angular pitch and orbital velocities into account it does not incorporate orbital radius, which is also obviously relevant. In order to address these issues the problem was reconsidered by Ziegler and Cartmell [summarised in Ref. [38] from work originally carried out by Ziegler and subsequently reported in full in Ref. [39]], with the overall geometry given in Figure 7.14(a). The general equation for the radius r on an elliptical orbit is given by,

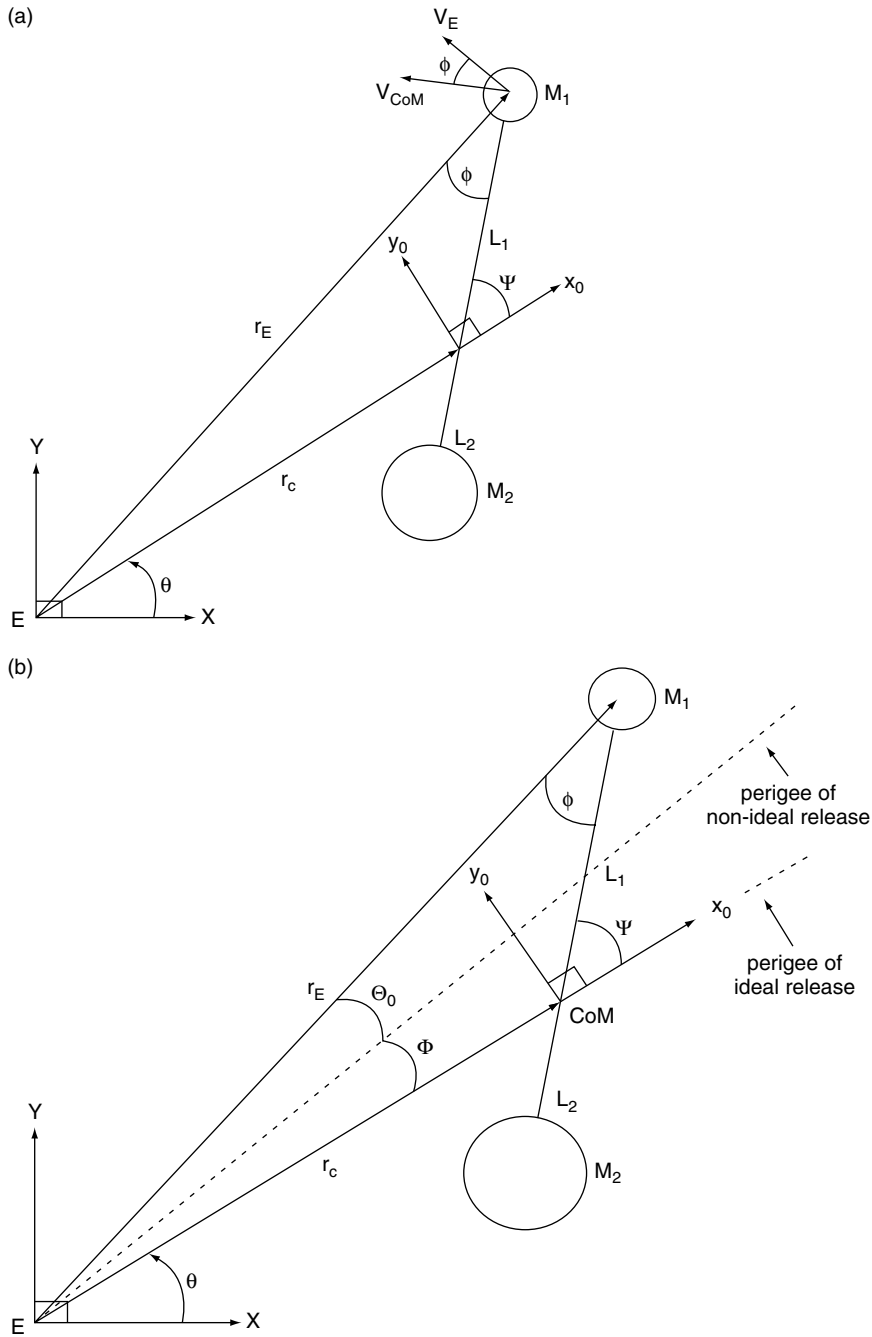$$r = \frac{p}{1 + e\cos\Theta} \tag{7.35}$$

(a)

(b)

Fig. 7.14. (a) Payload release geometry [39]. (b) Perigees for ideal and non-ideal payload release [39].

[55] from which the semilatus rectum, p, is given by the following,

$$p = a(1 - e^2) = \frac{b^2}{a} = r_p(1 + e) = r_a(1 - e), \tag{7.36}$$

where a is the semi-major axis, b is the semi-minor axis, e is the orbital eccentricity, Θ is the true anomaly, r_a is the apogee radius, and r_p is the perigee radius (or *apoapsis* and *periapsis* in a non-Earth centred system). The *total* release velocity, V_{Tot}, for the payload can be obtained in terms of the distance from the Earth's centre, E, to the payload, r_E, the semi-major axis of the orbit, a, and μ (where $\mu = GM_{\text{Earth}}$), from the vis-visa equation,

$$V_{\text{Tot}} = \sqrt{\mu\left(\frac{2}{r_E} - \frac{1}{a}\right)}. \tag{7.37}$$

This can be rearranged to obtain a for later use,

$$a = \frac{\mu r_E}{2\mu - V_{\text{Tot}}^2 r_E}. \tag{7.38}$$

The distance from the centre of the Earth, E, to the payload, M_1 is directly obtained from the geometry of Figure 7.14(a),

$$r_E = \sqrt{r_c^2 + L_1^2 + 2r_c L_1 \cos \Psi}, \tag{7.39}$$

noting that r_c is the circular orbit radius from E to the CoM and that L_1 is not necessarily equal to L_2. The total payload velocity comprises the following components,

$$V_{\text{Tot}} = \sqrt{V_R^2 + V_N^2} \tag{7.40}$$

where V_R and V_N are the radial and normal components, respectively. The radial velocity (pointing inwards to E) is given by,

$$V_R = V_{\text{CoM}} \sin \phi \tag{7.41}$$

The normal velocity component is the sum of the payload's orbital velocity, V_E, and a component of the tangential payload velocity relative to the CoM, V_{CoM}, and this acts in the direction of V_E. Therefore we obtain,

$$V_N = V_E + V_{\text{CoM}} \cos \phi \tag{7.42}$$

and the velocities V_E and V_{CoM} are given by,

$$V_E = r_E \dot{\theta} \quad \text{and} \tag{7.43}$$

$$V_{\text{CoM}} = L_1 \dot{\Psi}. \tag{7.44}$$

Since $\dot{\theta} = \sqrt{\mu/r_c^3}$ [55] this can be substituted into Eq. (7.43). The angle, ϕ, between V_{CoM} and V_E is obtained from the sine rule, as, $\frac{r_E}{\sin(\pi - \Psi)} = \frac{r_c}{\sin \phi}$, therefore,

$$\phi = \sin^{-1}\left(\frac{|r_c|}{|r_E|} \sin \Psi\right). \tag{7.45}$$

Now, substituting (7.43–7.45) into (7.41), the equation for V_R, and then into (7.42), the equation for V_N, those two velocities emerge as follows, after dropping the moduli for brevity,

$$V_R = \frac{L_1 r_c}{r_E} \dot{\Psi} \sin \Psi \tag{7.46}$$

$$V_N = r_E \sqrt{\frac{\mu}{r_c^3}} + L_1 \dot{\Psi} \cos \left[\sin^{-1} \left(\frac{r_c}{r_E} \sin \Psi \right) \right] \tag{7.47}$$

From Eq. (7.36) we can obtain e directly,

$$e = \sqrt{1 - \frac{p}{a}} \tag{7.48}$$

Also, the semilatus rectum, p, can be defined from standard analysis in terms of specific angular momentum, H, [55] thus,

$$p = \frac{H^2}{\mu} = \frac{(V_N r_E)^2}{\mu} \tag{7.49}$$

noting that H is the magnitude of the specific angular momentum given by $H = r_E^2 \dot{\theta}$ [55]. It has already been stated that the optimum release for a payload is when the tether is aligned along the local gravity vector, and therefore for the UP at the perigee (periapsis) of the released payload's elliptical orbit. This is along the $ECoMx_0$ line in Figure 7.14(b). The dotted line shows an alternative, non-ideal release orientation when the payload, M_1 lies on that line. Clearly, $\Psi - \phi = \Theta_0 + \Phi$, so we rearrange to get,

$$\Phi = \Psi - \phi - \Theta_0. \tag{7.50}$$

The apogee (or, more generally, the apoapsis) of an orbit-raised payload represents the location between an incoming payload and possibly the catching end of another tether. In order to obtain the orbital radius of a non-optimally released payload at the location of the required ideal apogee (apoapsis) the orbit's true anomaly defining this position will be,

$$\Theta_{\Delta\pi, apo} = \pi - \Phi. \tag{7.51}$$

7.6.2.5 Hanging tether

The optimum release position for a hanging tether is when the system is aligned along the local gravity gradient and because it is not librating or spinning, $\Psi = \dot{\Psi} = 0$. Calculating r_π from Eq. (7.35) allows us to obtain,

$$\Delta r_\pi = r_\pi - r_c, \tag{7.52}$$

where

$$r_\pi = r_{apo}. \tag{7.53}$$

After some algebra (inserting Eq. (7.36), Eqs. (7.38–7.40), and Eqs. (7.46–7.49) into Eq. (7.35)) the altitude gain for the upper payload for the hanging tether is given by,

$$\Delta r_\pi = \frac{(r_c + L)^4}{2r_c^3 - (r_c + L)^3} - r_c. \tag{7.54}$$

The altitude loss for the lower payload for the hanging tether is,

$$\Delta r_\pi = \frac{(r_c - L)^4}{2r_c^3 - (r_c - L)^3} - r_c. \tag{7.55}$$

For the case when the tether is swinging or spinning (both prograde), i.e., when $\dot{\Psi} \neq 0$, and when it is instantaneously coincident with the local gravity vector, then the altitude gain and loss, respectively, are given by,

$$\Delta r_\pi = \frac{(r_c + L)^2 \left[(r_c + L)\dot{\theta} + L\dot{\Psi}\right]^2}{2\mu - (r_c + L)\left[(r_c + L)\dot{\theta} + L\dot{\Psi}\right]^2} - r_c \tag{7.56}$$

$$\Delta r_\pi = \frac{(r_c - L)^2 \left[(r_c - L)\dot{\theta} - L\dot{\Psi}\right]^2}{2\mu - (r_c - L)\left[(r_c - L)\dot{\theta} - L\dot{\Psi}\right]^2} - r_c \tag{7.57}$$

We continue to assume that $L << r_c$, so if $\delta = \frac{L}{r_c}$ then $\delta << 1$, and applying a binomial expansion to Eqs. (7.54–7.57) can lead to simplified results identical to the literature results quoted in Eqs. (7.29) and (7.34); refer to Ziegler [39] for full details and to Ziegler and Cartmell for a summary [38]. From this it becomes clear that the best payload raising performance for a hanging tether is when it is closest to the Earth and as long as possible. Conversely the best payload de-boosting performance for a hanging tether is when it is as far as possible from the Earth and the tether is very long. The best performance obtainable from a prograde librating tether used for payload raising is for the largest possible libration angle and tether length, and for the system located as close to the Earth as possible. De-boost is optimized for the same system but located as far as possible from the Earth. In the case of a spinning (possibly motorized) tether then the situation is more complex, with various possibilities arising. The most important general conclusion is that an UP could be propelled from circular LEO to GEO using a long motorized system [39].

7.7 Tethers in orbit

7.7.1 Strength & materials

7.7.1.1 Terrestrially located hanging tether

We start off by considering a simple hanging tether located on Earth. Full weight is experienced at the support and zero weight at the free end below, so, the tether tension is given by $T = \left(\frac{m}{l}\right)zg$, where $0 \leq z \leq l$, and m/l equals mass per unit length, which is

constant for a chosen material. The tension varies linearly along the length of the tether, and if we write $\frac{m}{l}$ as $\hat{\rho}$, then,

$$T = \hat{\rho} l g. \tag{7.58}$$

This implies that there must be a critical value of length beyond which the tether will break due to its own weight. This is known as the *break-length*, l_*. Using this allows us to re-write Eq. (7.58) as,

$$T_* = \hat{\rho} l_* g, \tag{7.59}$$

where T_* is the *break tension*. These quantities were formally introduced by Beletsky and Levin in their seminal text [56]. So, re-arranging Eq. (7.59) leads to an expression for break-length,

$$l_* = \frac{T_*}{\hat{\rho} g} \tag{7.60}$$

and if we also introduce the *specific strength*, σ_*,

$$\sigma_* = \frac{T_*}{A}, \tag{7.61}$$

where A is the cross-sectional area of the tether, then we get the following,

$$l_* = \frac{\sigma_*}{\left(\frac{\hat{\rho}}{A}\right) g}, \tag{7.62}$$

where $\rho = \dfrac{\hat{\rho}}{A}.$ \hfill (7.63)

So, $l_* = \dfrac{\sigma_*}{\rho g}$ \hfill (7.64)

The specific strength, σ_*, has units of N/m^2 or Pa, and ρ is the material density in kg/m^3. Therefore, l_*, the break length, is a function of specific strength and density, and is effectively a *strength-to-density* ratio. We have assumed that stress is distributed uniformly over the tether cross-section but this depends on the homogeneity of the material and the design although it is a generally accepted assumption. Note also that the mechanics of the preceding analysis are purely terrestrial, therefore l_* is the break length *on Earth*.

7.7.1.2 Hanging tether in space

The next stage in the development is to consider a massive satellite in a circular orbit deploying a tether whose other end is free and orientated 'downwards' towards the Earth. For an orbital angular velocity of Ω, Beletsky and Levin [56] give the tension at the attachment point as,

$$T = \frac{3}{2}\hat{\rho} \Omega^2 l^2 = \frac{3}{2}\frac{m}{l} l^2 \Omega^2 = \frac{3}{2} m l \Omega^2 \tag{7.65}$$

with $l = 2l_\text{subspan}$, where l_subspan is half the total length of the tether, so this could also be expressed as, $T = 3ml_\text{subspan}\Omega^2$, to which we return at the end of Section 7.1.2. Adopting the same approach as before leads to an *orbital break tension* given by,

$$T_* = \frac{3}{2}\hat{\rho}\Omega^2 L_*^2 \tag{7.66}$$

reverting to Beletsky and Levin's notation [56].

Rearranging this gives the *orbital break length*,

$$L_* = \frac{1}{\Omega}\sqrt{\frac{2T_*}{3\hat{\rho}}}. \tag{7.67}$$

So if we re-use Eq. (7.61) we get,

$$L_* = \frac{1}{\Omega}\sqrt{\frac{2\sigma_* A}{3\hat{\rho}}} = \frac{1}{\Omega}\sqrt{\frac{2\sigma_*}{3\left(\frac{\hat{\rho}}{A}\right)}} = \frac{1}{\Omega}\sqrt{\frac{2\sigma_*}{3\rho}}. \tag{7.68}$$

Clearly, $L_* > l_*$, and in geostationary orbit it is even bigger and defined as $L_{*(\text{geo})}$, where $\Omega = \Omega_\text{geo}$.

Geostationary orbit is of interest for the *Space Elevator* application (a tether from the surface of the Earth to geostationary orbit). Table 7.1 is adapted from data given by Beletsky and Levin [56] and shows increasing break-lengths in descending order for four selected materials.

Note that a tether longer than L_*, for some chosen material, cannot even carry its own weight, let alone any cargo or payload. A relatively new material which can now be produced in quantity is *Spectra 2000*, which has a lower density than any of the above ($970\,\text{kg/m}^3$) and a specific strength of about 3.5 GPa. For geostationary orbit, where the orbital rate, Ω_geo, is 0.0000727 rad/s, the orbital break length of *Spectra 2000* is 21461 km. This is approximately half-way back from geostationary orbit to Earth, which compares to only a third of the way back for *Kevlar*. In fact there are no mass produced materials yet capable of supporting the Space Elevator. Carbon nanotubes are of considerable speculative interest, but economical mass production technologies have yet to be developed.

Table 7.1
Potential tether material properties.

Material	ρ [kg/m^3]	σ_* [GPa]	E [GPa]	l_* [km]	L_* [km]	$L_{*(\text{geo})}$ [km]
Tungsten	19300	4.0	410	21	320	5100
HP steel	7900	4.0	210	52	502	8000
Kevlar	1450	2.8	130	197	981	15700
Graphite	2200	20	690	928	2129	34100

7.7.1.3 Mass considerations

The *breaking mass* M_* can be defined as an upper limit for an application, therefore $M_T \leq M_*$. The mass of the tether can be defined by,

$$M_T = \rho k_a A l \tag{7.69}$$

for which Beletsky and Levin [56] define the constant k_a as,

$$k_a = \frac{d_T^2}{d_f^2 n} \tag{7.70}$$

noting that d_T and d_f are the diameters of the overall tether and the individual fibers, respectively, and n is the number of fibers that make up the multi-line tether. Equation (7.69) can be slightly revised to define the breaking-mass, $M_* = \rho k_a A L_*$, which rearranges to $\frac{M_*}{A} = \rho L_*$ if $k_a = 1$ (for the conceptually simple single line tether case). The previous table allows us to calculate this ratio of break-mass to tether cross-sectional area based on the values given for the density, ρ, and break-length, L_* for selected materials. Assuming a 1000 kg break-mass for an installation using *Kevlar*, we get a commensurate cross-sectional area of 0.7 mm^2 for the tether ($d_T = 0.944$ mm). Preserving this area, and looking at high performance steel and graphite, their associated break-masses for the same cross-section can be evaluated, $M_{*(\text{highperfsteel})} = 2776$ kg and $M_{*(\text{graphite})} = 3278$ kg. Clearly Spectra 2000 scores highly in comparison, with a break-length between *Kevlar* and graphite, but a density considerably lower than *Kevlar*.

7.7.2 Gravity gradient stabilisation for hanging tethers

An object of mass m, and radial position r from the centre of the Earth, and orbiting the Earth, is subjected to a gravitational force,

$$\mathbf{F}_G = -\frac{\mu m}{r^2}\mathbf{u}_r, \text{ with scalar form, } F_G = -\frac{\mu m}{r^2}, \tag{7.71}$$

where the unit vector $-\mathbf{u}_r$ refers to the fact that the gravity force is directed radially inwards. The inward acting centripetal force on the body is,

$$\mathbf{F}_C = -mr\Omega^2\mathbf{u}_r, \text{ with scalar form, } F_C = -mr\Omega^2. \tag{7.72}$$

A *hanging* tethered dumb-bell in a circular orbit travels along the orbital path with all points on the tether moving with the same velocity. The Centre of Mass (COM) of the tether will experience exactly enough gravitational pull to provide the centripetal force necessary for that radial position, therefore the gravitational force from Eq. (7.71) produces the centripetal acceleration. For a dumb-bell the outer end-mass is at a higher altitude and will therefore not feel sufficient gravity to provide the centripetal force consistent with the orbital velocity (which is the same as that of the COM due to the tether). Therefore $F_G < F_C$ and the outer end-mass will try to move outwards, generating a tension in the outer sub-span of the tether. The inner end-mass, however, feels too much gravity for the centripetal force required at that point, so $F_G > F_C$, and the inner end-mass tends to try to move further inwards. This generates a tension in the inner

sub-span. Therefore, at the COM ($r = r_0$) we can equate the scalar forms of Eqs. (7.71) and (7.72) to get,

$$-\frac{\mu m}{r_o^2} = -mr_0\Omega^2, \text{ and rearrangement gives, } \mu = \Omega^2 r_0^3. \tag{7.73}$$

Taking two cases either side of the COM for the dumb-bell, starting first with the outer case, for which, in general, $|F_G| < |F_C|$ and $r = r_0 + z$.

$$\therefore -\frac{\mu m}{r^2} = -mr\Omega^2 + F_{Zout}, \tag{7.74}$$

where m is the mass at r. Substituting for r and μ (from Eq. (7.73)) leads to,

$$F_{Zout} = m\Omega^2 \left((r_0 + z_{out}) - \frac{r_0^3}{(r_0 + z_{out})^2} \right) \tag{7.75}$$

and $z = z_{out}$, which is a point along the tether on the outer side of the COM. This resultant force is F_{Zout}. The quantities in the brackets in Eq. (7.75) can be expanded, and as $r_0 + z_{out} = r$ then the expansion becomes, $z_{out} + \frac{r_0 z_{out}(r_0 + r)}{r^2}$. If $r \to r_0$, implying a relatively short tether, then the bracketed term becomes, $z_{out} + \frac{r z_{out}(2r)}{r^2}$. This is equal to $3z_{out}$. The net tensile force F_{Zout} is outwards acting and so Eq. (7.75) reduces to,

$$F_{Zout} = 3mz_{out}\Omega^2, \text{ in the limit } r \to r_0 \text{ (i.e., for short tethers).} \tag{7.76}$$

For the inner case we have, $|F_G| > |F_C|$ and $r = r_0 - z$, but as we are using the COM as the datum for z_{out} and z_{in} we can put $-z = z_{in}$, since z_{in} is measured inwards, so $r = r_0 + z_{in}$.

$$\therefore -\frac{\mu m}{r^2} = -mr\Omega^2 - F_{Zin}. \tag{7.77}$$

Substituting for r and μ (from Eq. (7.73)) leads to,

$$F_{Zin} = m\Omega^2 \left(\frac{r_0^3}{(r_0 + z_{in})^2} - (r_0 + z_{in}) \right). \tag{7.78}$$

The quantities in the brackets can be expanded by using $r_0 + z_{in} = r$, and then letting $r \to r_0$, so that the expansion simplifies to $-3z_{in}$. This means that the net tensile force given in Eq. (7.78) can be reduced to,

$$F_{Zin} = -3mz_{in}\Omega^2, \text{ in the limit } r \to r_0 \text{ (i.e., for short tethers)} \tag{7.79}$$

Note that these are approximations which assume 'short' tethers and are commonly used in the tether literature [51, 56]. These *gravity gradient forces*, $F_{Zout} = 3mz_{out}\Omega^2$ and $F_{Zin} = -3mz_{in}\Omega^2$ define the tensile forces in each sub-span from $0 \leq |z_{out}| \leq l$ and $0 \leq |z_{in}| \leq l$. Therefore, for a symmetrical system, at any point equidistant from the COM on either side, $|F_{Zout}| = |F_{Zin}|$, and so the tensions are the same in each sub-span. Note here that total (payload-to-payload) tether length $L = 2l$, which is directly analogous to $l = 2l_{\text{subspan}}$ when referring to Beletsky and Levin's analysis [56] (see Section 7.7.1).
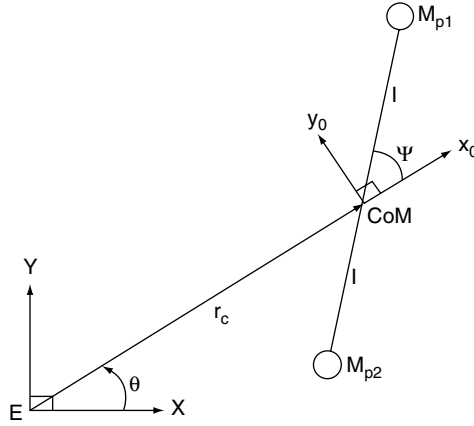
Fig. 7.15. Planar tether co-ordinate system.

7.7.3 Fundamental dynamical models for dumb-bell tethers

7.7.3.1 Planar tether on a circular orbit

Figure 7.15 shows a planar dumb-bell tether in the orbital plane. *EXY* is an Earth centered frame which is assumed to be inertial for this analysis, and *CoMx₀y₀* is a rotating frame whose origin is at the geometrical center, assumed coincident with the CoM. The tether sub-span lengths are equal and defined by l. The payload masses are equal such that $M_{P1} = M_{P2} = M_P$. The distance from the centre of the Earth E to the tether CoM is defined by the position vector, of magnitude r_c and true anomaly θ. The planar spin angle, or *pitch-angle*, is Ψ. This system is sufficient to construct a basic equation of motion for a passive planar dumb-bell tether, but by means of a relatively small extension to the modelling it is also possible to introduce an active motor drive to the tether by means of a conceptualized motor, gearbox, and counter inertia. On that basis the mass of a central facility containing the motor drive, gearboxes, power supplies, control systems, etc., needs to be defined and M_M is introduced for this. However, the counter-inertia does not need to be considered explicitly here, as long as it is appreciated that it would be necessary for any motor driven tether, and that it could take the form shown in the *outriggers* of Figure 7.16. Irrespective of whether or not the passive or motorized tether is pursued, the equation of motion for spin about the CoM can readily be obtained by deriving the system energies and then applying Lagrange's Equation.

The Cartesian positions of the principal components with respect to E are given as follows, assuming that the tether mass is located at $\frac{l}{2}$ on each side of the CoM,

$$x_{P1} = r_c \cos\theta + l\cos(\Psi+\theta), \quad y_{P1} = r_c \sin\theta + l\sin(\Psi+\theta),$$

$$x_{P2} = r_c \cos\theta - l\cos(\Psi+\theta), \quad y_{P2} = r_c \sin\theta - l\sin(\Psi+\theta),$$

$$x_M = r_c \cos\theta, \; y_M = r_c \sin\theta, \quad x_{T1} = r_c \cos\theta + \frac{l}{2}\cos(\Psi+\theta), \tag{7.80}$$
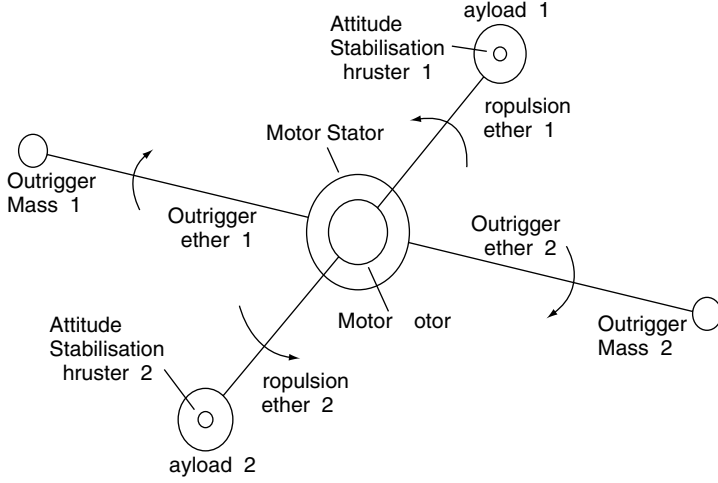
Fig. 7.16. Plan schematic of contra-rotating motorised tether components.

$$y_{T1} = r_c \sin \theta + \frac{l}{2} \sin(\Psi + \theta), \quad x_{T2} = r_c \cos \theta - \frac{l}{2} \cos(\Psi + \theta),$$

$$y_{T2} = r_c \sin \theta - \frac{l}{2} \sin(\Psi + \theta),$$

where subscripts $T1$ and $T2$ refer to positions halfway along the tether from the COM on each side and $P1$ and $P2$ denote payloads 1 and 2, respectively.

The system kinetic energy is easily constructed,

$$T = \frac{1}{2} M_P(\dot{x}_{P1}^2 + \dot{y}_{P1}^2) + \frac{1}{2} M_P(\dot{x}_{P2}^2 + \dot{y}_{P2}^2) + \frac{1}{2} M_M(\dot{x}_M^2 + \dot{y}_M^2) + \frac{1}{2} \rho Al(\dot{x}_{T1}^2 + \dot{y}_{T1}^2)$$
$$+ \frac{1}{2} \rho Al(\dot{x}_{T2}^2 + \dot{y}_{T2}^2) + \frac{1}{2}(2I_P + 2I_T + I_M)(\dot{\theta} + \dot{\Psi})^2, \tag{7.81}$$

where the mass moments of inertia about the local z-axes (component z-axes normal to the orbital plane of the system) are given by,

$$I_P = \frac{1}{2} M_P r_P^2, \tag{7.82}$$

$$I_T = \frac{1}{12} \rho Al(3r_T^2 + l^2), \tag{7.83}$$

$$I_M = \frac{1}{2} M_M r_M^2 \tag{7.84}$$

noting that I_T is the standard result for a solid circular section tether with axis normal to the orbital plane at $\frac{l}{2}$. Differentiating Eqs. (7.80) with respect to time and then substituting these velocities, and also Eqs. (7.82)–(7.84), as appropriate, into Eq. (7.81) leads to,

$$
T = \left(M_P + \rho A l + \frac{M_M}{2} \right) (\dot{r}_c^2 + r_c^2 \dot{\theta}^2)
$$
$$
+ \left(M_P \left[l^2 + \frac{r_p^2}{2} \right] + \frac{M_M r_M^2}{4} + \frac{\rho A l}{12} [4L^2 + 3r_T^2] \right) (\dot{\theta} + \dot{\Psi})^2 \tag{7.85}
$$

Note that for a circular orbit the quantities r_c and $\dot{\theta}$ represent a constant orbital radius and angular velocity, so these are not generalized coordinates in the Lagrangian sense and therefore $r_c = C_1$, $\dot{r}_c = 0$, $\dot{\theta} = C_2$, where C_1 and C_2 are constants, with C_2 disappearing from the analysis from hereon. C_1 is retained as r_c. The potential energy is based on the local position vectors from E to M_{P1} and M_{P2}, the position vector, r_c, between E and the CoM, and an appropriate integration along the sub-span lengths of the tether, thus,

$$
U_{P1} = -\frac{\mu M_P}{\sqrt{r_c^2 + l^2 + 2r_c l \cos \Psi}}, \tag{7.86}
$$

$$
U_{P2} = -\frac{\mu M_P}{\sqrt{r_c^2 + l^2 - 2r_c l \cos \Psi}} \tag{7.87}
$$

$$
U_M = -\frac{\mu M_M}{r_c} \tag{7.88}
$$

$$
U_{T1} = -\mu \rho A \int_0^l (r_c^2 + z^2 + 2r_c z \cos \Psi)^{1/2} dz \tag{7.89}
$$

$$
U_{T2} = -\mu \rho A \int_0^l (r_c^2 + z^2 - 2r_c z \cos \Psi)^{1/2} dz, \tag{7.90}
$$

where z is distance along each sub-span from the CoM outwards. Performing the integrations in Eqs. (7.89) and (7.90) leads to analytical forms for the potential energy contributions of the tether sub-spans, as follows,

$$
U_{T1} = \mu \rho A \ln \frac{r_c(1 + \cos \Psi)}{l + r_c \cos \Psi + \sqrt{r_c^2 + l^2 + 2r_c l \cos \Psi}} \tag{7.91}
$$

$$
U_{T2} = \mu \rho A \ln \frac{r_c(1 - \cos \Psi)}{l - r_c \cos \Psi + \sqrt{r_c^2 + l^2 - 2r_c l \cos \Psi}} \tag{7.92}
$$

Differentiating the energy functions for use with Lagrange's equation generates the equation of motion. Lagrange's equation is applied in the form,

$$\frac{\mathrm{d}}{\mathrm{d}t}\left(\frac{\partial T}{\partial \dot{q}}\right) - \frac{\partial T}{\partial q} + \frac{\partial U}{\partial q} = Q_q, \tag{7.93}$$

where Q_q is the generalized force associated with coordinate q, which in this case is $q \equiv \Psi$. Note that at this level of modelling if we require to incorporate the motor drive then the generalized force term is given simply by,

$$Q_\Psi = \tau \tag{7.94}$$

where τ is the applied torque in Nm. Therefore, applying Eq. (7.93) leads to the equation of motion for the motor driven system,

$$
\begin{aligned}
&\left(\frac{M_m r_m^2}{2} + M_p(2l^2 + r_p^2) + \frac{\rho Al[4l^2 + 3r_T^2]}{6}\right)\ddot{\Psi} \\
&\quad + \frac{\mu M_p r_c l \sin \Psi}{(r_c^2 + l^2 - 2r_c l \cos \Psi)^{3/2}} - \frac{\mu M_p r_c l \sin \Psi}{(r_c^2 + l^2 + 2r_c l \cos \Psi)^{3/2}} \\
&\quad - \mu\rho A \frac{r_c^2 + l^2 - r_c l(1 - \cos \Psi) + (l - r_c)\sqrt{r_c^2 + l^2 + 2r_c l \cos \Psi}}{r_c^2 + l^2 + 2r_c l \cos \Psi + (l + r_c \cos \Psi)\sqrt{r_c^2 + l^2 + 2r_c l \cos \Psi}}\tan\left(\frac{\Psi}{2}\right) \\
&\quad + \mu\rho A \frac{r_c^2 + l^2 - r_c l(1 + \cos \Psi) + (l - r_c)\sqrt{r_c^2 + l^2 - 2r_c l \cos \Psi}}{r_c^2 + l^2 - 2r_c l \cos \Psi + (l - r_c \cos \Psi)\sqrt{r_c^2 + l^2 - 2r_c l \cos \Psi}}\cot\left(\frac{\Psi}{2}\right) \\
&= \tau
\end{aligned}
\tag{7.95}
$$

This is a non-linear ordinary differential equation, with the non-linearities coming in from the potential terms. The inertia term, although algebraically complicated, is in fact linear in this model. This equation can be solved by numerical integration and this can be readily demonstrated using the *TetherSim* animated simulation [57]. In *TetherSim* the tether cross-section is assumed to be tubular (and not solid as defined above), so there is an inner radius, r_{Ti}, and an outer radius, r_{To}, within the expression for I_T in Eq. (7.83), so $(r_{T0}^2 + r_{Ti}^2)$ replaces r_T^2. *TetherSim* is based on a set of user-definable data with defaults given by the following, $\mu = 3.9877848 * 10^{14}\,\mathrm{m^3 s^{-2}}$, $M_p = 1000\,\mathrm{kg}$, $M_M = 5000\,\mathrm{kg}$, $r_M = r_p = 0.5\,\mathrm{m}$, $l = 50\,\mathrm{km}$, $r_c = 6870\,\mathrm{km}$, $r_{To} = 0.006\,\mathrm{m}$, $r_{Ti} = 0.004\,\mathrm{m}$, $A = 62.83\,\mathrm{mm^2}$, $\rho = 970\,\mathrm{kg/m^3}$ (Spectra 2000), $\sigma = 3.25\,\mathrm{GPa}$ (Spectra 2000), and a safety factor of 2 for the allowable tether strength. The initial conditions that are used are taken from Ziegler and Cartmell [38],

$$\Psi(0) = -0.9\,\mathrm{rad}, \quad \dot{\Psi}(0) = 0\,\mathrm{rad/s}. \tag{7.96}$$

It should be noted that the *TetherSim* graphics may occasionally run slowly, dependent on the connection to the server. The interested user is recommended to start with the default data, for which the motorized tether will librate, and then to change one parameter at a time in order to explore other aspects of the dynamics. Clearly the easiest way of getting monotonic spin-up for a chosen set of design data is to merely increase the motor

torque, but this may not always be the most desirable approach and in such situations a multi-variable optimization of the design may well be preferable.

7.7.3.2 Non-planar dumb-bell model

Having discussed the planar model on a circular orbit in Section 7.7.3.1, a non-planar model can be proposed next, once again using the *geocentric co-ordinate system*, as shown in Figure 7.17, and the governing equations of motion for a dumb-bell tether capable of operating out of the orbital plane can be derived. This is summarized from original work by Ziegler, first published within work by Cartmell et al. [58] and then in full by the originator [39]. In this section, R is used to represent the radius vector to the centre of mass of the orbiting tether system, and r_P, can be used to define the radius vector to the perigee of the orbit. The representation of Figure 7.17 is sufficient to define completely the system based on the Earth centre location, E, representing the origin of the X, Y, Z system, and the origin of the relative rotating x_0, y_0, z_0 co-ordinate system located at the centre of mass of the tether system, as in section 7.7.3.1. The X, Y plane and the x_0, y_0 plane lie on the orbital plane and the Z and z_0 axes are perpendicular to this. The X axis is directed to the orbit perigee and x_0 rotates in axial alignment with R. The in-plane angle, previously defined as the planar spin, or pitch angle, ψ, is now re-defined as the angle from the x_0 axis *to the projection of the tether onto the orbital*
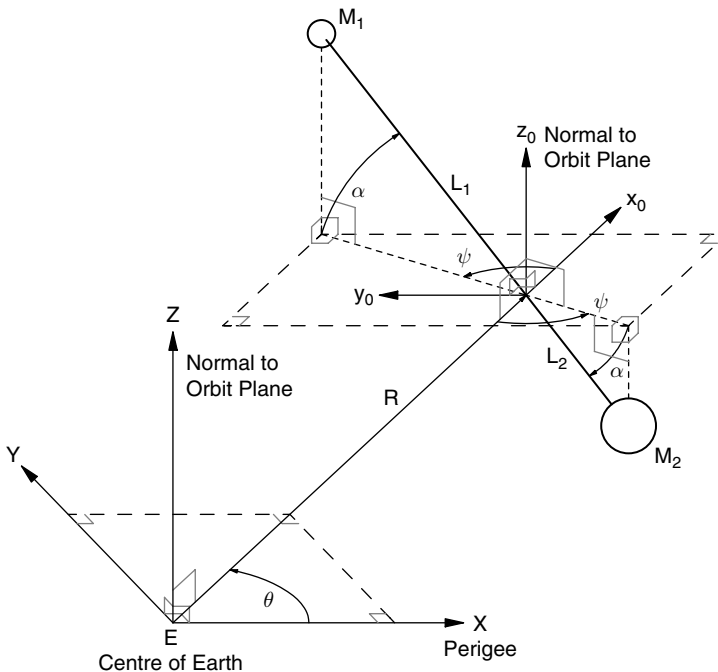

Fig. 7.17. Non-planar tether co-ordinate system [39, 58].

plane. In addition to this an out-of-plane angle, α, goes from the tether to its projection onto the orbital plane, and is always normal to the orbital plane.

The equations of motion are once again obtained by means of the Lagrangian approach. The system consists of two end masses, M_1 and M_2, connected by a tether with sub-span lengths denoted by L_1 and L_2. The Earth's gravitational field is assumed to be spherical, and there are negligible environmental perturbations, rigid tethers with constant cross-sectional area and negligible mass compared to that of the payloads (for simplicity). As in Section 7.7.3.1 the Cartesian positions are obtained, this time in the following forms,

$$x_1 = R\cos\theta + L_1\cos\alpha\cos(\psi + \theta)$$
$$y_1 = R\sin\theta + L_1\cos\alpha\sin(\psi + \theta)$$
$$z_1 = L_1\sin\alpha$$
$$x_2 = R\cos\theta - L_2\cos\alpha\cos(\psi + \theta)$$
$$y_2 = R\sin\theta - L_2\cos\alpha\sin(\psi + \theta)$$
$$z_2 = -L_2\sin\alpha. \tag{7.97}$$

In this case R, θ, α, ψ are regarded as the generalized co-ordinates, and the positions of the payloads with respect to the centre of the Earth are given by,

$$R_1 = \sqrt{x_1^2 + y_1^2 + z_1^2} = \sqrt{L_1^2 + R^2 + 2L_1 R\cos\alpha\cos\psi} \tag{7.98}$$

$$R_2 = \sqrt{x_2^2 + y_2^2 + z_2^2} = \sqrt{L_2^2 + R^2 - 2L_2 R\cos\alpha\cos\psi}. \tag{7.99}$$

The kinetic energy of the system in terms of the payloads and neglecting the tether can be expressed by translational point-mass payload components,

$$T = \frac{1}{2}M_1\left(\dot{x}_1^2 + \dot{y}_1^2 + \dot{z}_1^2\right) + \frac{1}{2}M_2\left(\dot{x}_2^2 + \dot{y}_2^2 + \dot{z}_2^2\right), \tag{7.100}$$

where the dot once again denotes differentiation with respect to time. Differentiating equations (7.97) with respect to time and substitution, as appropriate, into Eq. (7.100) gives the following, assuming moment equilibrium $M_1 L_1 = M_2 L_2$,

$$T = \frac{1}{2}(M_1 + M_2)(\dot{R}^2 + R^2\dot{\theta}^2) + \frac{1}{2}(M_1 L_1^2 + M_2 L_2^2) \times [\dot{\alpha}^2 + \cos^2\alpha\,(\dot{\psi} + \dot{\theta})^2] \tag{7.101}$$

Neglecting the tether mass, the potential energy of the payloads is given by,

$$U = -\frac{\mu M_1}{R_1} - \frac{\mu M_2}{R_2}. \tag{7.102}$$

Substituting (7.98) and (7.99) into Eq. (7.102) gives the system's potential energy,

$$U = -\frac{\mu M_1}{\sqrt{L_1^2 + R^2 + 2L_1 R\cos\alpha\cos\psi}} - \frac{\mu M_2}{\sqrt{L_2^2 + R^2 - 2L_2 R\cos\alpha\cos\psi}}. \tag{7.103}$$

Given that the length of a typical tether is likely to be two to three orders of magnitude less than the orbital radius then its potential energy can be expanded with $\delta_1 = \frac{L_1}{R}$ and $\delta_2 = \frac{L_2}{R}$, where $\delta_1 \ll 1$ and $\delta_2 \ll 1$. On the assumption that $M_1 L_1 = M_2 L_2$, expansion up to $O(\delta_1^3)$ and $O(\delta_2^3)$ leads to,

$$
U = -\frac{\mu (M_1 + M_2)}{R} + \frac{\mu \left(M_1 L_1^2 + M_2 L_2^2\right)\left(1 - 3\cos^2\alpha\cos^2\psi\right)}{2R^3}
$$
$$
-\frac{\mu\left(M_1 L_1^3 - M_2 L_2^3\right)\left(3\cos\alpha\cos\psi - 5\cos^3\alpha\cos^3\psi\right)}{2R^4}
\tag{7.104}
$$

The kinetic and potential energies in Eqs. (7.101) and (7.104) are substituted into Lagrange's equation in the required multi-degree of freedom form,

$$
\frac{\mathrm{d}}{\mathrm{d}t}\left(\frac{\partial T}{\partial \dot{q}_i}\right) - \frac{\partial T}{\partial q_i} + \frac{\partial U}{\partial q_i} = Q_{q_i} \quad i = 1, 2, \ldots, N,
\tag{7.105}
$$

where, in this case, the generalized forces Q_{q_i} are zero because no external forces or torques are assumed here (such as were provided by the motor drive in Section 7.7.3.1). Applying Eq. (7.105) leads to four equations of motion governing motion through the in and out-of-plane angles defined for the tether, the true anomaly, and the radial distance from the focus of the elliptical orbit to the center of mass of the tether. Alternatively, standard orbital mechanics relationships [55] can be used to transform the equations from the time domain to the true anomaly domain, thereby simplifying them algebraically, and also reducing the number of equations down from four to two by assuming a circular orbit, for which $e = 0$, resulting in,

$$
\psi'' - 2\alpha'\tan\alpha\,(\psi' + 1) + \frac{3}{2}\sin(2\psi) + \frac{3(L_1 + L_2)\sin\psi\sec\alpha}{2r_C}
$$
$$
\times\left(1 - 5\cos^2\psi\cos^2\alpha\right) = 0,
\tag{7.106}
$$

$$
\alpha'' + \frac{1}{2}\sin(2\alpha)\left[(\psi' + 1)^2 + 3\cos^2\psi\right] + \frac{3(L_1 - L_2)}{2r_C}\cos\psi\sin\alpha
$$
$$
\times\left(1 - 5\cos^2\psi\cos^2\alpha\right) = 0.
\tag{7.107}
$$

It is important to note that the prime represents differentiation with respect to the true anomaly and the dot denotes differentiation with respect to time, and that this is opposite to the convention used in Cartmell et al. [58]. Equations (7.106) and (7.107) could be solved numerically, however Ziegler offers approximate analytical solutions (within the review by Cartmell et al. [58] and in full within Ref. [39]) by means of the multiple scales perturbation scheme applied up to third-order perturbation accuracy and also by expanding the trigonometrical functions by means of the Taylor series and retaining the first two terms. The multiple scales solution is uniformly valid close to $\psi = \alpha = 0$. In the case of numerical integration solutions the simplifying expansion of the potential energy

expression is not required and so Eq. (7.103) can be used instead to lead to alternative forms for the two governing equations, as follows,

$$
\psi'' - 2\tan\alpha\,\alpha'\,(\psi'+1) + \frac{r_C^4}{L_1+L_2}\sin\psi\sec\alpha\left[\left(r_C^2+L_2^2-2r_C L_2\cos\psi\cos\alpha\right)^{-3/2}\right.
$$
$$
\left. -\left(r_C^2+L_1^2+2r_C L_1\cos\psi\cos\alpha\right)^{-3/2}\right]=0 \tag{7.108}
$$

$$
\alpha'' + \frac{1}{2}\sin(2\alpha)\,(\psi'+1)^2 + \frac{r_C^4}{L_1+L_2}\cos\psi\sin\alpha\left[\left(r_C^2+L_2^2-2r_C L_2\cos\psi\cos\alpha\right)^{-3/2}\right.
$$
$$
\left. -\left(r_C^2+L_1^2+2r_C L_1\cos\psi\cos\alpha\right)^{-3/2}\right]=0. \tag{7.109}
$$

Equations (7.108) and (7.109) can be numerically integrated and their solutions compared with the approximate analytical solutions to Eqs. (7.106) and (7.107) (which are not given here but discussed in full by Ziegler [39] and partly reproduced by Cartmell et al. [58]). The approximate solution to third-order perturbation must be differentiated with respect to the true anomaly to evaluate the constants of integration at $\theta = 0$ for zero initial velocity conditions for each angle [39, 58]. The value chosen for the low Earth orbit radius, r_C, is taken to be 7000 km, and very short tether lengths are used, $L_1 = L_2 = 500$ m, thereby ensuring that the potential energy expansion conditions are properly satisfied. Figures 7.18 and 7.19 illustrate the response obtained between the fourth and fifth orbit in an attempt to magnify the discrepancies between the solutions. It can be seen that these are relatively marginal and that for the data used the third-order multiple scales solutions approximate the numerical integrations results quite well. Further work on non-planar models using non-equatorial elliptical orbits has shown the potential for extremely complex three-dimensional motions [40] in which there is scope for very considerable inter-coordinate coupling and highly non-linear dynamical behavior. The circular restricted three-body
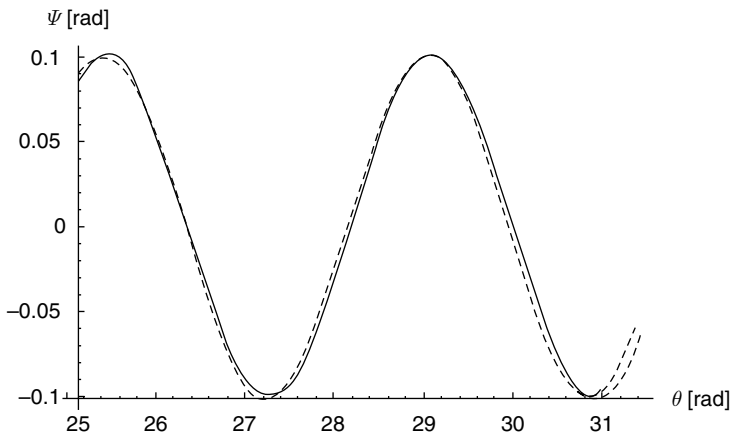

Fig. 7.18. Response of angle ψ as a function of true anomaly θ, solid line—numerical solution, dashed line—second-order multiple scales solution, chain dashed line—third-order multiple scales solution [39, 58].
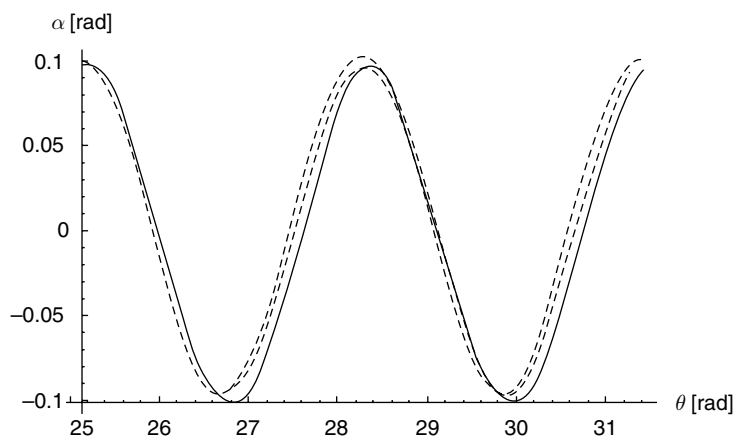
Fig. 7.19. Response of angle α as a function of true anomaly θ, solid line—numerical solution, dashed line—second-order multiple scales solution, chain dashed line—third-order multiple scales solution [39, 58].

problem can be used (the third body is the Sun), in order to permit a weak stability boundary transfer via Lagrange point L_1 and this in conjunction with a non-equatorial orbit for a pair of staged passive tethers is shown to be potentially capable of Earth–Moon payload transfer for realistic tethers and significant payload masses (typically 500 kg each). The work reported in [40] is based on pragmatically sized tethers working in a staged configuration at the Earth end (see next section for a discussion on staging) and a long Moravec Lunavator tether depositing and retrieving payloads to and from the lunar surface.

7.7.4 Payload exchange concepts

Hoyt and Forward [59] first suggested that doubled-up, staged, tethers could be used from SEO to LTO for transfers of payloads between the Earth and the Moon by using mass balance to ensure conservation of momentum throughout. The method links the *Sub-Earth-orbit to LEO* method of Carroll [60] to the *EEO to LTO* proposal of Stern [61]. Cartmell & Ziegler [42] applied this to the motorized momentum exchange concept and then Cartmell et al. [40] presented some preliminary calculations for a lunar transfer through L_1 on the basis of non-equatorial tether orbits around Earth in order to obviate the need for a plane change at the Moon end. On reaching the Moon payloads are captured by a Moravec Lunavator [34], which brings the payload round from LLO and down to the Lunar surface. The reverse is also possible in principle. Clearly the appropriate orbital elements must be calculated to make payload handovers occur when there is instantaneous zero relative velocity at the points where the payload is to be transferred during its journey. Initially, the payload is boosted up to SEO by means of chemical propulsion to rendezvous with the LEO tether in a slightly elliptical orbit, after which tether propulsion takes over, first by means of the staged tether rendezvous and boost through to LTO, passage through
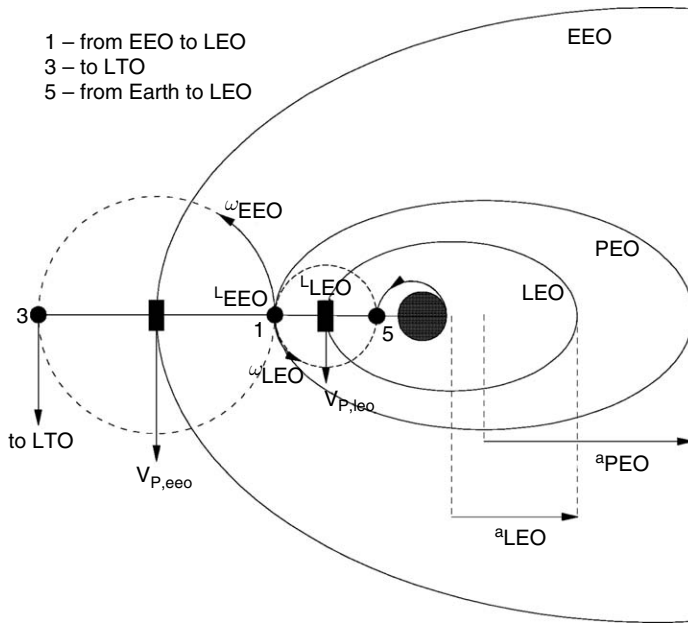
Fig. 7.20. Staged tethers shown at alignment [42].

L_1, with sufficient energy to continue to the Moon and capture by a Moravec Lunavator. Effects of gravitational perturbations on the tethers due to other bodies, and the Earth's oblateness, have both been neglected in analyses to date. Figure 7.20 shows the instant when the two staged tethers are in alignment. The inner tether is on LEO and the outer tether is on EEO. There are two emergency payload capture orbits, PEO, and PEO_1 (not shown). In principle this approach could be used with passive momentum exchange tethers, but the control and logistics required, and the maximizing of available energy levels for optimal performance, suggest that motorized tethers would be the best solution. The concept is based on the continual and synchronized arrival and departure of payloads of identical mass flowing in and out of the system, thereby ensuring that each tether is alternately either fully laden with two payloads, or completely unladen on both sides. It also assumes that suitable technologies will be in place for payload handovers, major orbital maintenance in the event of missed handovers (and therefore asymmetrically laden tethers and unattached payloads moving along their rescue orbits), solar electric power supplies, control and logistics, and of course an appropriate manufacturing or habitation infrastructure which requires to exploit two-way mass movement between the planets. Figure 7.20 shows the instant at which the payload labelled 5 has just been delivered from SEO to the right-hand end of the LEO tether (looking down onto the system) under conditions of zero relative velocity at that point. At this precise moment the EEO tether passes payload 1 inwards to the left-hand side of the LEO tether, so that the LEO tether is simultaneously loaded at each end. At that same moment the EEO tether releases payload 3 into LTO. This means that the EEO tether is unladen at both ends at exactly the same

time that the LEO tether is fully laden at both ends. The step changes in mass moment of inertia of the two tethers will have a potential de-orbiting effect and work is in hand to quantify this at the time of writing. The orbit periods are harmonic, and this and the facility spin rate determines when the necessary handover conditions can occur. If the handover fails another attempt may be possible the next time they come round. This potential problem arises for transfers from SEO to LEO, and vice versa, and also from LEO to EEO, and vice versa. In the next stage payload 1 comes to rendezvous with the Earth transfer vehicle on a return SEO. Meanwhile payload 5 is handed over from the LEO tether to the EEO tether to collect payload 6 (not shown in Figure 7.20). Payload 6 could have been in PEO_1 instead, perhaps due to a missed capture first time round. Assuming handovers occur as planned the LEO tether becomes empty as the EEO tether becomes full. The SEO booster brings payload 7 (also not shown in Figure 7.20) up to the LEO tether and the EEO tether hands over payload 6. The EEO tether also releases payload 5 into LTO. Thus, the EEO tether empties and the LEO tether fills. This all charts the progress of payload 5 from SEO to LTO, and the logical process can continue indefinitely as long as payloads continue to arrive at the right time and place. The above shows that flows of payload can be arranged into and out of the staged tether system so that neither of the two tethers is ever asymmetrically laden. A full analysis of this is given by Cartmell and Ziegler [42] and Cartmell et al. [40] in which it is shown that this concept, when used with pragmatic data can readily generate Earth escape velocities for reasonable tether geometries and mass characteristics.

7.8 Conclusions

Solar sailing and space tethers both offer exciting new possibilities for the future by either extracting momentum from the environment, or balancing momentum through payload exchanges. These novel propulsion technologies offer many interesting new avenues of research in orbital dynamics, some of which have been discussed here. For solar sailing, the continuous thrust generated by the sail allows exotic new families of highly non-Keplerian orbits, while staged tether systems allow intriguing means of transferring payloads at essentially no cost. While some of these possibilities have been discussed here, it is clear that there are many unexplored opportunities which await investigation in the future. In particular, future technology developments may allow solar sails to be fabricated with a sail lightness number of order one. This would provide a continuous thrust of the same order as the local solar gravitational acceleration, surely enabling interesting new families of orbit. Similarly, developments in carbon nanotubes may provide tethers with remarkable mechanical properties, allowing extremely large loads to be transferred to high energy orbits.

Lastly, it is surely through the novel features of the orbital mechanics of these propellantless propulsion systems that further compelling practical applications will arise, which will in turn unlock the resources to meet the engineering challenges they present. While the underlying orbital mechanics may be interesting and exciting, implementation is the key to the future.

References

1. Tsiolkovsky, K.E. (1921). *Extension of Man into Outer Space* [also, Tsiolkovsky, K.E. (1936), Symposium Jet Propulsion, No. 2, United Scientific and Technical Presses].

2. Tsander, K. (1924). *From a Scientific Heritage*, NASA Technical Translation TTF-541, 1967 [quoting a 1924 report by the author].

3. Friedman, L., et al. (1978). Solar sailing—the concept made realistic. AIAA-78-82, AIAA Aerospace Sciences Meeting, Huntsville.

4. McInnes, C.R., Macdonald, M., Angelopolous, V. and Alexander, D. (2001). GeoSail: exploring the geomagnetic tail using a small solar sail. *Journal of Spacecraft and Rockets*, **38**, pp. 622–629.

5. West, J.L. and Derbes, B. (2000). Solar sail vehicle system design for the geostorm warning mission. AIAA-2000-5326, AIAA Structures, Structural Dynamics and Materials Conference and Adaptive Structures Forum, Atlanta.

6. Macdonald, M., McInnes, C.R. and Hughes, G.W. (2004). A near-term roadmap for solar sailing. IAC 04-U.1.09, 55th International Astronautical Congress, Vancouver.

7. Sauer, C.G. (1999). Solar sail trajectories for solar polar and interstellar probe missions. AAS-99-336, AAS/AIAA Astrodynamics Specialist Conference, Gridwood, Alaska.

8. Dachwald, B. (2004a). Optimal solar sail trajectories for missions to the outer solar system. AIAA-2004-5406, AIAA/AAS Astrodynamics Specialist Conference, Providence.

9. McInnes, C.R., Hughes, G. and Macdonald, M. (2003), Low cost mercury orbiter and mercury sample return missions using solar sail propulsion. *The Aeronautical Journal*, **107**, pp. 469–478.

10. Hughes, G.W. and McInnes, C.R. (2004). Small-body encounters using solar sail propulsion. *Journal of Spacecraft and Rockets*, **41**, pp. 140–150.

11. McInnes, C.R. (2004). Deflection of near-earth asteroids by kinetic energy impacts from retrograde orbits. *Planetary and Space Science*, **52**, pp. 587–590.

12. McInnes, C.R. (1999a). *Solar Sailing: Technology, Dynamics and Mission Applications*, Springer-Verlag, London.

13. Murphy, D.M. and Murphey, T.W. (2003). Scalable solar-sail subsystem design concept. *Journal of Spacecraft and Rockets*, **40**, pp. 539–547.

14. Salama, M., White, C. and Leland, S. (2003). Ground demonstration of a spinning solar sail deployment concept. *Journal of Spacecraft and Rockets*, **40**, pp. 9–14.

15. McNeal, R., Hedgepeth, J.M. and Schuerch, H.U. (1969). Heliogyro solar sailer summary report. NASA Contractor Report CR-1329.

16. Coverstone-Carroll, V. L. and Prussing, J. E. (2003). Technique for Escape from Geosynchronous Transfer Orbit Using a Solar Sail. *Journal of Guidance, Control, and Dynamics*, **26**(4), pp. 628–634.

17. McInnes, C.R. (2002). Solar sailing: orbital mechanics and mission applications. COSPAR02-A-03497, 53rd International Astronautical Federation Congress, Houston.

18. Bacon, R.H. (1959). Logarithmic spiral—an ideal trajectory for an interplanetary vehicle with engines of low sustained thrust. *American Journal of Physics*, **27**, pp. 12–18.

19. Tsu, T.C. (1959). Interplanetary travel by solar sail. *American Rocket Society Journal*, **29**, pp. 422–427.

20. London, H.S. (1960). Some exact solutions of the equations of motion of a solar sail with a constant setting. *Journal of the American Rocket Society*, **30**, pp. 198–200.

21. Sauer, C.G. (1976). Optimum solar sail interplanetary trajectories. AIAA-76-792, AAS/AIAA Astrodynamics Specialist Conference, San Diego.

22. Dachwald, B. (2004b). Optimization of interplanetary solar sailcraft trajectories using evolutionary neuro-control. *Journal of Guidance, Control, and Dynamics*, **27**(1), pp. 66–72.

23. Powers, B. and Coverstone-Carroll, V. (2001). Optimal solar sail orbit transfers to synchronous orbits. *Journal of the Astronautical Sciences*, **49**(2), pp. 269–281.

24. Forward, R.L. (1991). Statite: A Spacecraft that Does Not Orbit, *Journal of Spacecraft and Rockets*, **28**(5), pp. 606–611.

25. McInnes, C.R., McDonald, A.J.C., Simmons, J.F.L. and MacDonald, E.W. (1994). Solar sail parking in restricted three-body systems. *Journal of Guidance Dynamics and Control*, **17**, pp. 399–406.

26. McInnes, C.R. (1999b). Artificial lagrange points for a non-perfect solar sail. *Journal of Guidance, Control and Dynamics*, **22**, pp. 185–187.

27. McInnes, C.R. (2003). Solar sailing: mission applications and engineering challenges. Philosophical Transactions of the Royal Society A, **361**, pp. 2989–3008.

28. Farquhar, R.W., Muhonen, D.P. and Richardson, D.L. (1977). Mission design for a halo orbiter of the earth. *Journal of spacecraft and rockets*, **14**(3), pp. 170–177.

29. Tsiolkovsky, K.E. (1959). *Grezi o zemle i nene*, USSR Academy of Sciences Edition, p. 35. [also, Tsiolkovsky, K.E. (1961). *A Way to the Stars*, Izdatelstvo, AN SSSR], both in Russian.

30. Artsutanov, Yu. (1960). V kosmos na elektrovoze. *Komsomolskaya Pravda*.

31. Isaaks, J.D., *et al*. (1966). Satellite elongation into a true 'skyhook'. *Science*, **151**, pp. 682–683.

32. Colombo, G., Gaposchkin, E.M., Grossi, M.D. and Weiffenbach, G.C. (1975). The 'Skyhook': a shuttle-borne tool for low-orbital-altitude research. *Meccanica*, **10**, pp. 3–20.

33. Cosmo, M.L. and Lorenzini, E.C. (1997). Tethers in space handbook. 3rd edition, Smithsonian Astrophysical Observatory.

34. Moravec, H. (1977), A Non-synchronous Orbital Skyhook. *Journal of the Astronautical Sciences*, **25**, pp. 307–332.

35. Tethers Unlimited Inc. (2005). http://www.tethers.com/

36. Carroll, J.A. (1985). Guidebook for Analysis of Tether Applications. Final Report on Contract RH4-394049 for the Martin Marietta Corp.

37. Cartmell, M.P. (1998). Generating velocity increments by means of a spinning motorised tether. 34th AIAA/ASME/SAE/ASEE Joint Propulsion Conference and Exhibit, Cleveland, Ohio, USA, paper AIAA 98-3739.

38. Ziegler, S.W. and Cartmell, M.P. (2001). Using motorised tethers for payload orbital transfer. *AIAA Journal of Spacecraft and Rockets*, **38**(6), 904–913.

39. Ziegler, S.W. (2003). *The Rigid-Body Dynamics of Tethers in Space*, Ph.D. thesis, Department of Mechanical Engineering, University of Glasgow.

40. Cartmell, M.P., McInnes, C.R. and McKenzie, D.J. (2004). Proposals for an earth–moon mission design based on motorised momentum exchange tethers. XXXII Summer School on 'Advanced Problems in Mechanics', Russian Academy of Sciences, St. Petersburg, Russia.

41. McKenzie, D.J. and Cartmell, M.P. (2004). On the performance of a motorized tether using a ballistic launch method. 55th International Astronautical Congress 2004, Vancouver Convention and Exhibition Centre, Vancouver.

42. Cartmell, M.P. and Ziegler, S.W. (1999). The use of Symmetrically Laden Motorised Tethers for Continuous Two-way Interplanetary Payload Exchange. 35th AIAA/ASME/SAE/ASEE Joint Propulsion Conference and Exhibit, Bonaventure Hotel and Conference Center, Los Angeles, California, USA, paper AIAA 99-2840.

43. Delta Utec SRC, 2005, http://www.delta-utec.com/.

44. Lennert, S. and Cartmell, M.P. (2003). Analysis and design of a friction brake for momentum exchange propulsion tethers. Fifth IAA International Conference on Low-Cost Planetary Missions, ESA/ESTEC.

45. Ouyang, H., Mottershead, J.E., Cartmell, M.P. and Friswell, M.I. (1997). Parametric Resonances in an Annular Disc with a Rotating System of Distributed Mass and Elasticity; and Effects of Friction and Damping, *Proceedings of the Royal Society of London*, Series A, **453**, pp. 1–19.

46. NASA Science Mission Directorate (2005). http://www.inspacepropulsion.com/

47. Colombo, G., Martinez-Sanchez, M. and Arnold, D. (1982). The use of tethers for payload orbital transfer. Smithsonian Astrophysical Observatory, NAS8-33691, Cambridge, MA, USA.

48. Bekey, I. and Penzo, P.A. (1986). Tether propulsion. *Aerospace America*, **24**(7), pp. 40–43.

49. Kelly, W.D. (1984). Delivery and Disposal of a Space-Shuttle External Tank to Low Earth Orbit. *Journal of the Astronautical Sciences*, **32**(3), pp. 343–350.

50. Lorenzini, E.C., Cosmo, M.C., Kaiser, M., Bangham, M.E., Vonderwell, D.J. and Johnson, L. (2000). Mission Analysis of Spinning Systems for Transfers from Low Orbits to Geostationary. *Journal of Spacecraft and Rockets*, **37**(2), pp. 165–172.

51. Arnold, D.A. (1987). The behaviour of long tethers in space. *Journal of the Astronautical Sciences*, **35**(1), pp. 3–18.

52. Carroll, J.A. (1986). Tether Applications in Space Transportation. *Acta Astronautica*, **13**(4), pp. 165–174.

53. Bekey, I. (1983). Tethers open new space options. *Astronautics and Aeronautics*, **21**(4), pp. 32–40.

54. Kumar, K., Kumar, R. and Misra, A.K. (1992), Effects of deployment rates and librations on tethered payload raising. *Journal of Guidance, Control, and Dynamics*, **15**(5), pp. 1230–1235.

55. Chobotov, V.A. (1996). *Orbital Mechanics*, 2nd edition, AIAA Education Series, AIAA, Reston, VA, USA.
56. Beletsky, V.V. and Levin, E.M. (1993). *Dynamics of Space Tether Systems*, Advances in the Astronautical Sciences, **83**, American Astronautical Society, San Diego, CA, USA.
57. TetherSim (2002). Available by request from colin.mcinnes@strath.ac.uk.
58. Cartmell, M.P., Ziegler, S.W., Khanin, R. and Forehand, D.I.M. (2003). Mechanics of Systems with Weak Nonlinearities. Transactions of the ASME, Applied Mechanics Reviews, **56**(5), pp. 455–492.
59. Hoyt, R.P. and Forward, R.L. (1997). Tether transport from sub-earth-orbit to the lunar surface . . . and back!. International Space Development Conference, Orlando, Florida, USA.
60. Carroll, J.A. (1991). Preliminary design of a 1 km/s tether transport facility. Tether Applications Final Report on NASA Contract NASW-4461, with NASA/HQ.
61. Stern, M.O. (1988). Advanced propulsion for LEO-Moon transport. NASA CR-172084, California Space Institute progress report on NASA grant NAG 9-186, with NASA/JSC.